

Attachment A

Passive Gamma Logging at Probe Hole P9-20 OU 7-10 Staged Interim Action Project, Stage I

Pui Kuan

SUMMARY

The passive gamma measurements along probe hole P9-20 obtained by WMTS during the logging campaign at Pit 9 in January 2000 are examined in somewhat more detail than was reported in the logging report prepared by WMTS shortly after the logging campaign. This closer examination pays particular attention to the energy spectrum of the Pu-239 measurements along P9-20. In order to reproduce the measured energy spectrum, it is hypothesized that an absorbing layer lies between the plutonium contaminated waste and the gamma detector. This hypothesis also leads to the assumption that the waste could be displaced to one side of the probe tube instead of fully surrounding the tube, the latter being the geometry of the detector efficiency calibration performed by WMTS prior to the logging campaign. Based this assumed geometry, calculations are performed to match the measured gamma line intensities of Pu-239 at the 129, 204, 345, 375, and 414 keV energies at eight positions along the depth of P9-20. The calculations show that localized Pu-239 quantities of over 2 kg is consistent with the assumed geometry and the measurements. However, the estimated quantity of plutonium depends on waste geometry, which cannot be uniquely determined, given the limited number of measurement points. For certain waste configurations, e.g., uniform distribution around the probe tube, the measurements are also consistent with plutonium quantities on the order of 100 g.

CONTENTS

SUMMARY	iii
ACRONYMS	vii
1. INTRODUCTION.....	1
2. PASSIVE GAMMA LOGGING TOOL AND PROBE HOLE GEOMETRY.....	5
3. DETECTOR RESPONSE.....	6
4. LIMITATIONS OF THE WASTE MANAGEMENT TECHNICAL SERVICES CALIBRATION AND ANALYSIS PROCEDURE.....	7
5. METHODOLOGY TO DETERMINE CALIBRATION CORRECTION FACTORS	8
5.1 Self Absorption by Waste Matrix.....	8
5.2 Attenuation by an Intervening Layer between Waste and Probe Tube	8
5.3 Geometrical Effects	9
6. GAMMA RAYS FROM PLUTONIUM-239 DECAY	10
7. GAMMA RAY TRANSPORT AND DETECTOR RESPONSE	11
8. MEASUREMENT DATA	15
9. LOGGING RESULTS ANALYSIS.....	17
10. ESTIMATES OF PLUTONIUM-239 CONTENT ALONG PROBE HOLE.....	20
11. DISCUSSION	27
12. CONCLUSION	29
13. EPILOG	30
14. REFERENCES.....	32
Appendix A—Absolute Efficiencies of a 40% HPGe Detector	A-1
Appendix B—On the Derivation of Waste Distribution from Passive Gamma Measurements.....	B-1
Appendix C—Comments and Independent Estimates of Plutonium Content Around P9-20.....	C-1
Appendix D—Monte Carlo Calculation for a Specific P9-20 Waste Geometry.....	D-1

FIGURES

1-1.	Location of OU 7-10 Staged Interim Action Project Stage I Operations in Pit 9	2
1-2.	Map showing Pit 9 study area boundary and probe locations. Coordinates are based on RWMC site-specific coordinate system	3
7-1.	One-dimensional (slab) geometry of γ ray transport	12
8-1.	Gamma spectrum at the 4.97 ft depth along P9-20	15
9-1.	Apparent Pu-239 concentrations ($C\Omega$) along probe hole P9-20	18
9-2.	Calculated apparent Pu-239 concentrations ($C\Omega$) at the 6.97 ft level	19
10-1.	Geometry of a localized waste sphere	21
10-2.	Comparison of measured and predicted count rates for Pu-239 204 keV line	23
10-3.	Comparison of measured and predicted count rates of Pu-239 345 keV line	24
10-4.	Comparison of measured and predicted count rates of Pu-239 375 keV line	25
10-5.	Comparison of measured and predicted count rates of Pu-239 414 keV line	26

TABLES

1.	Gamma mass attenuation coefficients (cm^2/g)	8
2.	Spectral gamma lines from the decay of Pu-239	10
3.	Intrinsic efficiency of a 40% relative efficiency HPGe detector	13
4.	Count rates (counts per second) of P9-20 Pu-239 spectral lines	16
5.	Apparent Pu-239 concentrations along P9-20	17

ACRONYMS

DOE-ID	Department of Energy, Idaho Operations Office
EDF	Engineering Design File
EPA	Environmental Protection Agency
HPGe	High Purity Germanium
IDHW	Idaho Department of Health and Welfare
INEEL	Idaho National Engineering and Environmental Laboratory
keV	kilo-electron volts
MeV	million electron volts
OU	Operable Unit
RFP	Rocky Flats Plant
RWMC	Radioactive Waste Management Complex
SDA	Subsurface Disposal Area
SWEPP	Stored Waste Examination Pilot Plant
WMTS	Waste Management Technical Services

Passive Gamma Logging at Probe Hole P9-20 OU 7-10 Staged Interim Action Project, Stage I

1. INTRODUCTION

The staged Operable Unit 7-10 (OU 7-10) Staged Interim Action Project was jointly developed by the U.S. Department of Energy, Idaho Operations Office (DOE-ID), the Environmental Protection Agency (EPA) Region 10, and the Idaho Department of Health and Welfare (IDHW) to obtain characterization and bench and pilot scale treatability information in support of full assessment of radioactive and hazardous wastes buried in the Subsurface Disposal Area (SDA) located in the Radioactive Waste Management Complex (RWMC) at the Idaho National Engineering and Environmental Laboratory (INEEL). As part of the Stage I of the project, 20 probe holes were installed in a 40 × 40-ft area near the southwest end of Pit 9, where wastes from the Rocky Flats Plant (RFP) were buried in 1968.¹ Based on shipping records, the wastes were contained in 55-gal drums at the time of burial. Approximately 40% of these drums were empty, 20% contained combustibles (paper, rags, etc.), and 30% contained an organic sludge, referred to as 743 series sludge in the waste classification vernacular, from weapons material processing. Out of a total of 1307 drums disposed of in the probe area, there were 22 drums that contained graphite molds and 3 drums that contained 741 series sludge, the first stage sludge in the process of americium removal from plutonium at Rocky Flats. Measurements at the Stored Waste Examination Pilot Plant (SWEPP) at the INEEL of stored drums shipped after 1970 from the RFP show that the 741 and 743 series sludge, and the graphite mold wastes can contain a concentration of tens and even hundreds of grams of plutonium per waste drum.² It has not been established how representative these stored drums are of the drums buried in Pit 9 in 1968.

Logging activities were carried out in the 20 probe holes in January 2000. Logging instruments included a neutron-neutron moisture tool, a passive neutron detector, an activated gamma tool, a passive gamma detector, and a partially shielded gamma detector to determine the azimuthal dependence of passive gamma intensities around the probe hole. The objectives as well as preliminary logging results are documented in *OU 7-10 Initial Probing Campaign Downhole Logging Results*.³ A map of Pit 9 is shown in Figure 1-1 and the locations of the probe holes within the 40 × 40-ft subsurface exploration area are shown in Figure 1-2.

While the suite of logging tools provides a wealth of information regarding soil moisture, waste composition, particularly chlorine content, and radionuclide information, they have not been analyzed in detail to realize the full usefulness of the data except for a cursory examination of "hot" spots and general waste distribution. This lack of detailed analysis is understandable, given the voluminous data gathered and the short time period elapsed between the time of logging and the preparation of the logging results report. This Engineering Design File (EDF) is one of several attempts that selectively examine the logging results in more detail in order to gain a better understanding of the waste distribution in the exploration area. Specifically, this EDF addresses the potential plutonium contents around probe hole P9-20 based on the passive gamma log along P9-20.

The primary reason for choosing P9-20 for this analysis is the observation that the count rates of Pu-239 gamma lines along P9-20 are hundreds to thousands times higher than those measured along the other probe holes where Pu-239 gamma lines were detected. Analysis by the logging contractor, Waste Management Technical Services (WMTS), indicates that the Pu-239 concentration is in excess of 100,000 nCi/g at approximately 6 ft under the surface at the P9-20 location.⁴ At a specific activity of

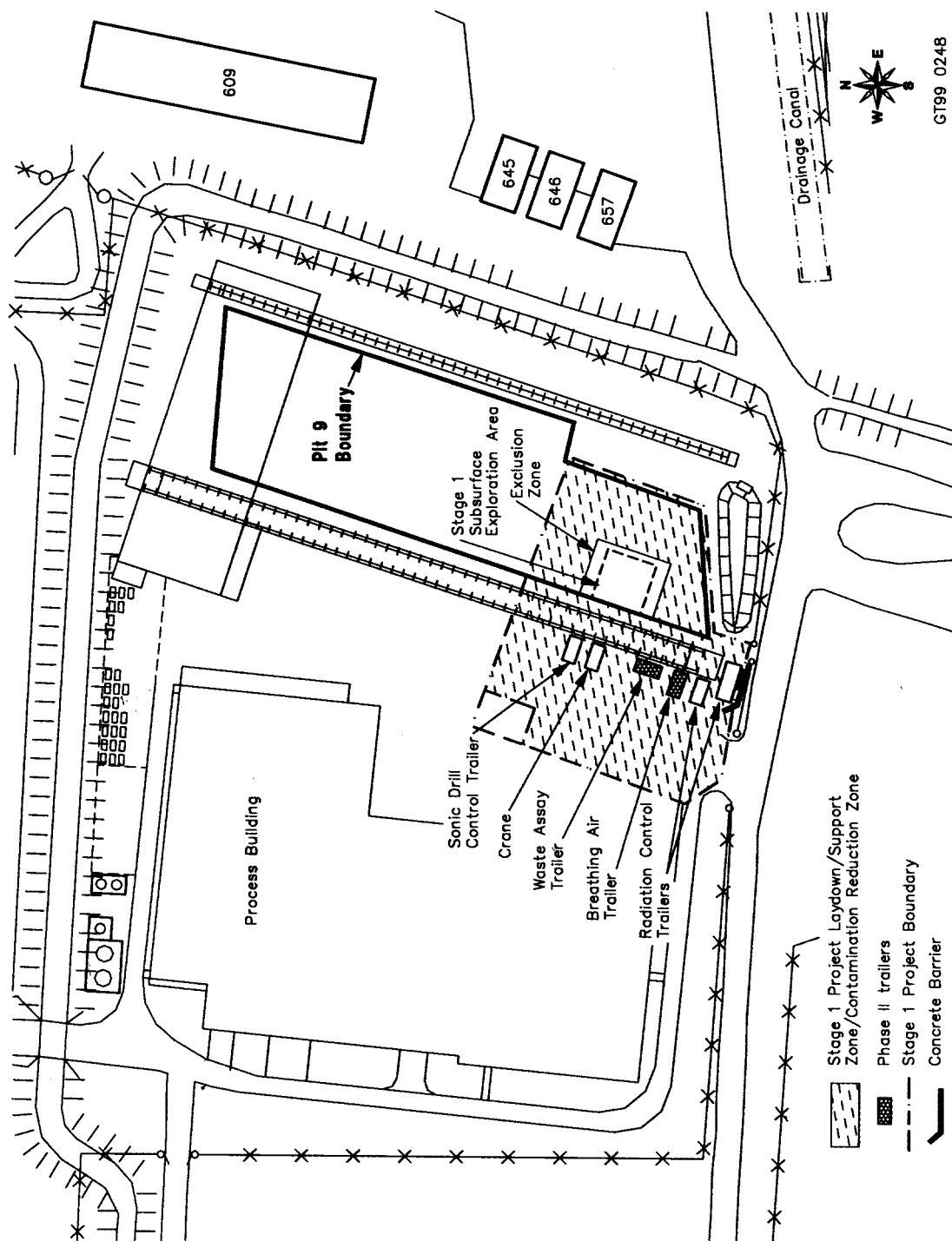


Figure 1-1. Location of OU 7-10 Staged Interim Action Project Stage I Operations in Pit 9.

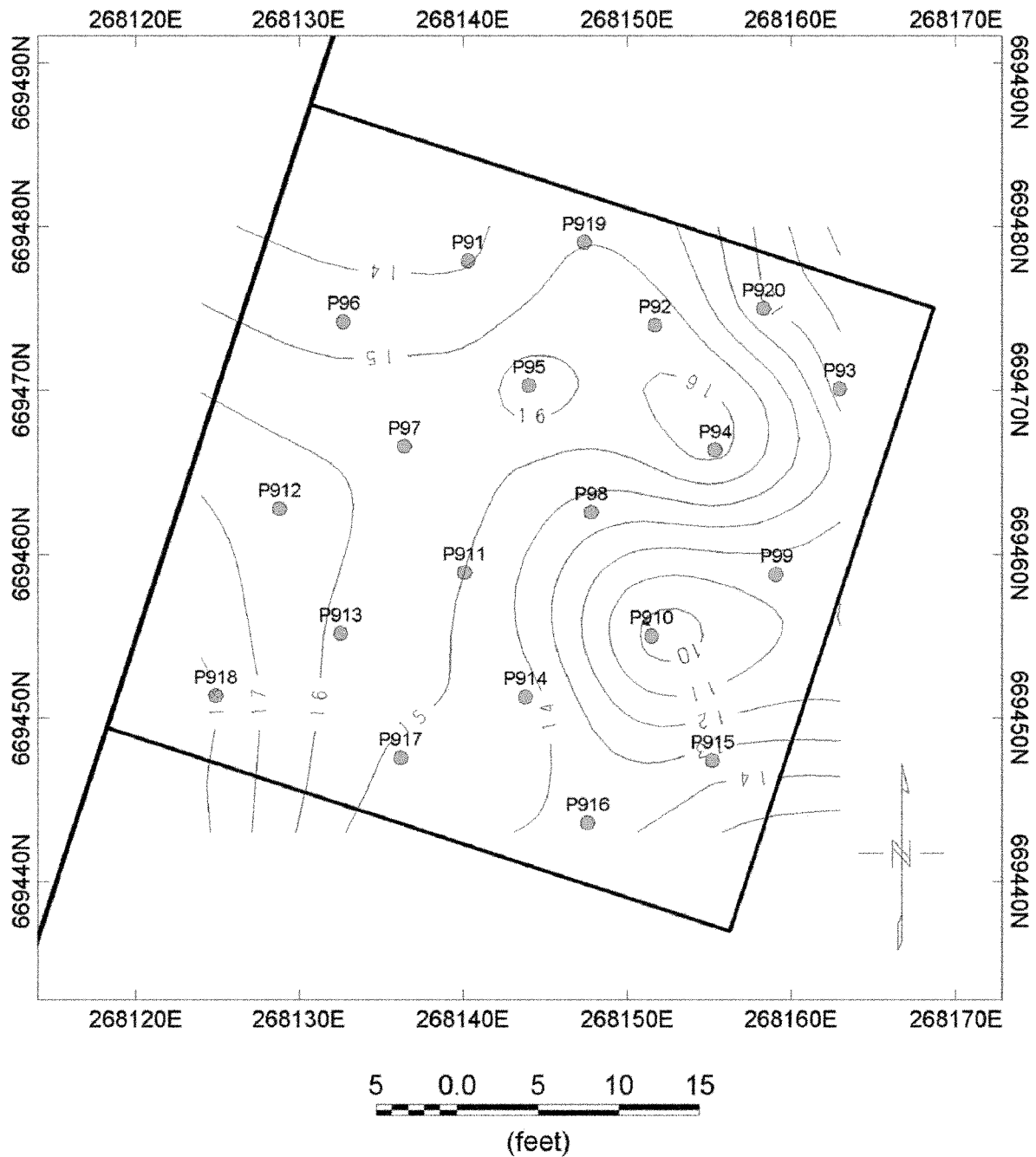


Figure 1-2. Map showing Pit 9 study area boundary and probe locations. Coordinates are based on RWMC site-specific coordinate system.

0.062 Ci per gram of Pu-239, the 100,000 nCi/g concentration translates to a 0.16% mass concentration of Pu-239 in the waste matrix. If the waste matrix has a mass on the order of 100 kg, then the Pu-239 content in that waste has a mass on the order of 160 g, an unusually high, but not inconceivable, value among all the transuranic waste drums stored aboveground at the RWMC within the INEEL.²

This EDF examines more closely the data obtained at P9-20, specifically, the spectral gamma intensities of Pu-239. Unlike the method used by WMTS to obtain the radionuclide concentration, which is solely based on calibration with a cylindrical matrix uniformly distributed around the detector, models of other subsurface waste distributions are also used to fit the data. Such models include the effect of soil absorption on the measurements, decrease in detector efficiency when the radiation does not impinge on the detector from all directions, and geometrical dilution of radiation when the source is localized in waste drums. All these effects, when they are present, tend to increase the calculated concentration in the waste matrix over that calculated from the WMTS calibration and will thus increase the calculated total amount of plutonium around the P9-20 hole. Conversely, when these effects are ignored in their presence, the calculated amount of plutonium under-estimates the amount that is actually present.

The following sections describe the passive gamma measurement, the method used by WMTS to arrive at the Pu-239 concentrations from the measurement results, an analytical approach to estimating the gamma radiation at the detector, and, with the use of calibrated detector efficiencies, a determination of the Pu-239 concentrations in the waste matrix. Models of the waste configuration are then used to reproduce the measurement of gamma count rates at various elevations along probe hole P9-20.

2. PASSIVE GAMMA LOGGING TOOL AND PROBE HOLE GEOMETRY

A 35% efficiency (relative to a standard sodium iodide crystal at 1.33 MeV) high purity germanium (HPGe) detector was used in the Pit 9 logging campaign to detect gamma rays emitted by radionuclides. The detector was lowered into the probe hole tube at 6-in. intervals. At each location, gamma rays were counted for 100 seconds. The actual counting time (live time) was generally less than the clock time because of limits in system response time. According to the logging contractor, WMTS, as long as the live time is over 68% of the clock time (32% dead time correction), the dead time correction is accurate and the count rate can be calculated by dividing the total count by the live time. At a few locations along the P9-20 hole, because of high gamma fluxes, the dead time corrections were much higher than 32%, and, consequently, the count rates, as calculated by dividing the actual number of counts by the live time, had large, unknown errors.

The probe tube is a 5-1/2 in. OD tube made of tool steel with a wall thickness of 1/2 in. The HPGe detector is approximately 2 in. in diameter, typical of a 35% HPGe detector, but its exact dimensions have not been obtained at this time. (As shown later in this EDF, when a normalization factor from the calibration is used to define the intrinsic efficiency of the detector, the actual size of the detector is immaterial in the calculations.)

3. DETECTOR RESPONSE

The detector has been calibrated against radionuclide concentrations in dry concrete matrices at the Hanford site. The concrete blocks are 4 ft in diameter and have uncased, 4-1/2-in. calibration holes along their central axes. The radionuclide (potassium, uranium, and thorium) enriched zones are 4 ft high. Therefore, a detector in the calibration hole receives radiation from an essentially infinite matrix in all directions. The Pit 9 count rate to concentration conversion factors are based on this calibration geometry, with corrections made for the presence of the 1/2-in. tool steel casing used at the Pit 9 site, while still assuming that the geometric arrangement and the matrix type are similar to those of the Hanford calibration models. Based on this procedure, WMTS reported a count rate to Pu-239 conversion factor of 68.84 nCi/g of Pu-239 in the contaminated soil matrix for each count per second (dead time corrected) under the photopeak of the 414-keV Pu-239 gamma line. This calibration factor will be used in normalizing the detector efficiency in subsequent calculations in this EDF.

4. LIMITATIONS OF THE WASTE MANAGEMENT TECHNICAL SERVICES CALIBRATION AND ANALYSIS PROCEDURE

In normal geophysical logging, the medium around the logging borehole is more or less homogeneous, at least on a scale that can influence detector response at each location. The calibration models used at Hanford for the Pit 9 gamma logging tool simulate this configuration. If the waste matrix is similar to the concrete used in the calibration in terms of gamma attenuation properties and the probe tube goes through the waste matrix, the calibration factor that relates the gamma count rates to radionuclide concentrations would be applicable and would yield fairly accurate radionuclide concentrations.

Based on disposal records, the waste in Pit 9 in the probing area were mostly contained in 55-gal drums and these drums were dumped in Pit 9. The space between drums was filled with soil. For any probing into Pit 9, there is no guarantee that the probe hole would go through a drum. Even if it does, there is no guarantee that that drum would contain measurable quantities of radionuclides. Therefore, in general, the measured radiation in a probe hole could come from radionuclides in a waste matrix that is separated from the outer surface of the probe tube by either a layer of soil or another waste matrix that contains little radionuclides.

The above discussion points to the need for several corrections to the calibration that converts count rates to radionuclide concentrations. These are listed below.

1. A correction factor should be evaluated using the gamma attenuation coefficients of the waste matrix instead of those for concrete that lead to the calibration curve.
2. Attenuation by an intervening layer and the waste matrix should be applied to obtain the true radiation intensity at the waste surface.
3. Allowance should be made for wastes that do not surround the probe tube but are located off to one side of the probe tube.

The next section presents the methodology used in this EDF to apply the above corrections to the calibration.

5. METHODOLOGY TO DETERMINE CALIBRATION CORRECTION FACTORS

5.1 Self Absorption by Waste Matrix

The simplest assumption about radionuclide distributions in a waste matrix is one of uniform distribution in a homogeneous waste matrix. For wastes having dimensions greater than a few inches in any one direction, radiation below 1 MeV in energy is greatly attenuated by the matrix itself and the emerging radiation flux (number of gamma rays per unit surface area) from the waste matrix is essentially independent of the size the matrix, but depends only on the mass absorption coefficient of the matrix. The statement will be elaborated quantitatively in subsequent analysis in this EDF. The assumption about uniform distribution and homogeneous matrix may be relaxed to include situations where the non-uniformity and non-homogeneity are limited to length scales less than the attenuation length of the radiation (length scale over which the radiation is attenuated by a factor of e , the base of natural logarithm).

Table 1 shows the mass attenuation coefficients of two waste forms (graphite and series 741 sludge), iron, and concrete, which is the matrix used in the physical calibration model. These attenuation coefficients are based on the elemental attenuation coefficients listed in the CRC Handbook of Chemistry and Physics.⁵ The attenuation coefficients are approximately the same for all the materials listed in the table except for energies close to 100 keV, where the attenuation coefficients are larger for materials that contain heavier elements. This result is due to the fact that in the energy range between 200 keV and 1 MeV, the attenuation is mostly due to Compton scattering by atomic electrons and the attenuation coefficients are proportional to the number of electrons per unit mass, which is approximately constant for elements from helium to iron. Because of such similarities in the attenuation coefficients, the matrix effect on the calibration is small when the medium is optically thick (dimensions greater than a length scale over which the radiation is attenuated by a factor of e , the base of natural logarithm). When the medium is optically thin (very little self-absorption), the emerging radiation is obviously independent of the medium because it has little effect on the radiation. Therefore, in general, the matrix effect on the emerging radiation can be ignored in the calibration unless very accurate results are desired.

Table 1. Gamma mass attenuation coefficients (cm^2/g).

Gamma Energy (keV)	Graphite	741 Sludge	INEEL Soil	Iron	Concrete ^a
100	0.151	0.205	0.176	0.372	0.175
200	0.123	0.132	0.128	0.146	0.127
500	0.087	0.089	0.088	0.084	0.088
1000	0.064	0.064	0.064	0.060	0.064

a. Assuming 31 wt% each for SiO_2 , Al_2O_3 , and CaCO_3 , and 7 wt% water.

5.2 Attenuation by an Intervening Layer between Waste and Probe Tube

The gamma detector is calibrated in an uncased hole through a concrete block, which contains radionuclides uniformly distributed throughout its volume. The detection efficiency of the radiation from a source is influenced by both the intrinsic efficiency of the detector (the detected fraction of gamma rays

that impinge on the detector) and the fraction of the radiation impinging on the detector. Gamma rays at different energies from a radionuclide are emitted in fractions of the number of decays of the radionuclide (absolute intensities). With no attenuation, the relative strengths of the detected gamma rays will be proportional to the absolute intensities multiplied by the detector efficiency at the respective energies. With matrix attenuation, these relative strengths are modified by the relative attenuation at the various energies. As discussed in Section 5.1, as long as the matrix is optically thick to these gamma rays, these relative strengths will be similar to those obtained in the concrete block calibrations because of the small variation of the attenuation coefficients with matrix type.

If the emitting medium is optically thin or if there is an intervening layer of absorbing material between the emitting medium and the probe tube, the strengths of the gamma rays from a nucleus at various energies in general will be different from the calibrated ratios. If the emitting medium is optically thin and there is no absorbing layer between the source and the detector, the ratio of the measured strength of a gamma ray at a lower energy to that at a higher energy will approach the ratios of the absolute intensities after correcting for the energy dependency of the detector efficiency. On the other hand, if the emitting medium is optically thick and/or there is an absorbing layer, the ratios will decrease because of the preferential absorption of low energy gamma rays.

The effect of an absorbing layer on the measured intensity ratios is used as the basis for deducing the presence of that layer. The thickness of the layer will be used as a parameter to reproduce the observed ratios. The most likely absorbing layer is soil and the attenuation coefficients of soil will be used in the calculations. However, the results are insensitive to the type of the assumed absorbing material because most materials have similar mass attenuation coefficients, including the various types of waste buried under Pit 9.

5.3 Geometrical Effects

The detector calibration is performed in a small hole inside a concrete block. Any point on the cylindrical surface of the detector receives radiation from the concrete essentially from a half space, i.e., a 2π solid angle. In addition, all surfaces of the detector receive radiation from the concrete matrix. In the Pit 9 logging operation, although the probe hole passing through a waste package is a possibility, which would mimic the calibration geometry, the general geometry is one that has a waste package displaced at a distance from the probe hole.

This general geometrical arrangement of the waste matrix introduces two effects on detecting the radiation from the waste matrix. First, only part of the detector surface receives unscattered radiation from the waste matrix. This reduces the effective surface area of the detector and thus its efficiency. Second, on any point of the detector surface that receives the radiation, the radiation will not be coming from a 2π solid angle, but rather from a reduced solid angle. This reduced solid angle is approximately the solid angle subtended at the detector by the projected area of the radiating surface perpendicular to the radius vector from the detector. Both the reduction in the effective area of the detector and the less than 2π solid angle of the radiating surface can greatly reduce the unscattered radiation received by the detector. Without correcting for these factors, the concentration of radionuclides in the waste matrix based on the well calibration can be grossly under-estimated.

6. GAMMA RAYS FROM PLUTONIUM-239 DECAY

Many gamma rays in the range between 100 keV and 500 keV from Pu-239 decay are detected in P9-20 logging. Some of the spectral lines are either too weak or blended with other lines to give reliable results, but a few spectral lines stand out clearly in the Compton-scattered gamma background. These spectral lines, along with their intensities defined as gamma rays per 100 Pu-239 decays, are given in Table 2, based on the WWW Table of Radioactive Isotopes.⁶

The gamma rays listed in the table will be used in this study to deduce the Pu-239 concentrations in a waste matrix based their count rates by the passive gamma detector.

Table 2. Spectral gamma lines from the decay of Pu-239.

Energy (keV)	Intensity (gammas per 100 decay)
129.3	6.31E-03
203.6	5.69E-04
345.0	5.56E-04
375.1	1.55E-03
413.7	1.47E-03

7. GAMMA RAY TRANSPORT AND DETECTOR RESPONSE

Because detector calibrations are performed with physical models that could be very different from a waste matrix in gamma ray transport properties, the calibrations can not be used directly to deduce accurate radionuclide concentrations in a waste. Instead, model calculations must be performed for specific waste types and geometries to properly interpret the measurement results. In this section, a simple one-dimensional gamma ray transport model is developed and an adjustment parameter is used to tie the results of the analytical model to the physical calibration of the detector. The analytical model is used in later sections to interpret the measurement results.

It is assumed that gamma transport is along a ray and only depends on the distance along the ray from its point of emission. Only gamma rays detected in the photopeaks are considered, so only emission and attenuation of gamma rays need to be included in the formulation. Any scattered (almost all Compton scattered) gamma ray is assumed not captured by the detector in the photopeak.

The radiation transport, including absorption and emission, but not scattering, is described by the following equation:⁷

$$\frac{dI_E}{dx} = -\kappa_E \rho I_E + j_E \rho \quad (7-1)$$

where I_E is the gamma ray intensity at energy E (number of gamma rays at energy E per unit time per unit area per unit solid angle), x is a length along the ray, κ_E is the mass attenuation coefficient, ρ is the density of the medium, and j_E is the emissivity (gamma rays per unit time per unit mass per unit solid angle). Equation (7-1) contains only one independent variable (x), but it can be applied to three dimensions, since x can be described by three co-ordinate positions. The geometry of the gamma ray transport in one-dimensional slab geometry is shown in Figure 7-1. Each ray is characterized by the directional angle, θ .

We consider a uniform source of emission in a waste matrix. Let C denote the concentration of the radionuclide in units of nano-Curie per gram mass of the matrix, then j_E is given by

$$j_E = (C/4\pi) \times 0.37 \times N_E \quad (7-2)$$

where N_E is the number of gamma rays at energy E for each 100 radionuclide decays. The factor 0.37 comes from a conversion factor from 1/100 nano-Curies to disintegrations per second. The factor 4π changes total emission over all directions to emission per unit solid angle.

In addition to the position-independent (within the waste) emission source term, we assume that the attenuation coefficient and the density are also position-independent. The transport equation then can be solved to give

$$I_E = (j_E / \kappa_E) [1 - \exp(-\kappa_E \rho L)] \quad (7-3)$$

where L is the distance from one edge of the waste to the opposite edge. Note that when the optical depth ($\kappa_E \rho L$) is large, the intensity is simply j_E / κ_E , which is independent of the density of the waste.

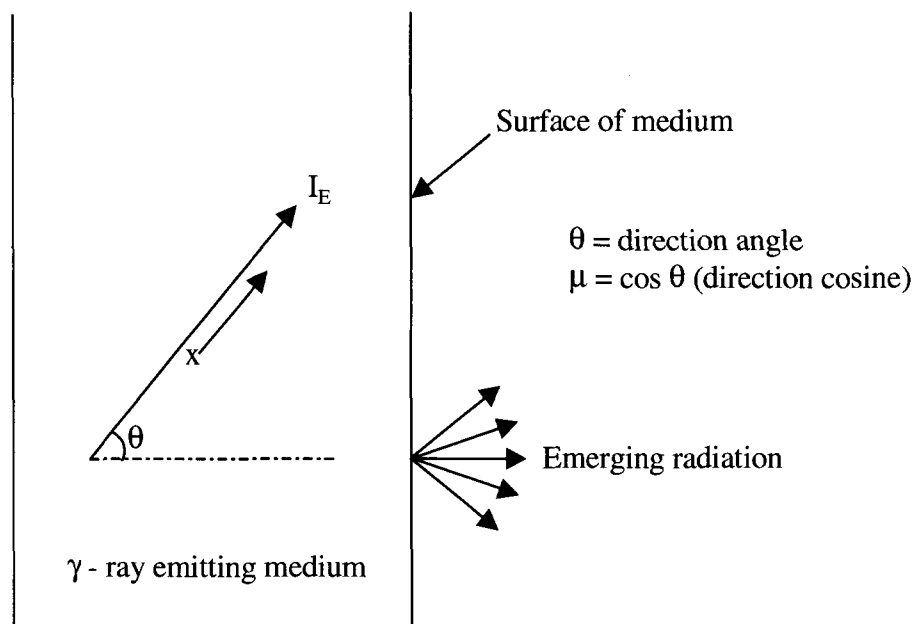


Figure 7-1. One-dimensional (slab) geometry of γ ray transport.

If there is an inert layer that contains no radionuclides between the waste and the detector, the attenuation of that layer has to be included in the above solution.

Let the subscripts "w", "i", and "s" denote waste, inert layer, and probe tube respectively. Then the general solution of the intensity along each ray is, again assuming constant attenuation and density parameters within each material,

$$I_E = (j_E / \kappa_{E,w}) [1 - \exp(-\kappa_{E,w} \rho_w L_w)] \exp(-\kappa_{E,i} \rho_i L_i) \exp(-\kappa_{E,s} \rho_s L_s) \quad (7-4)$$

The flux, F_E , of gamma rays crossing a unit surface area is obtained by integration over the solid angles over half a hemisphere:

$$F_E = 2\pi \int_0^1 I_E \mu d\mu \quad (7-5)$$

where μ is the direction cosine of the ray making with the normal of the surface. For the slab case, it is shown in Figure 7-1.

For intensities independent of direction, which is a good approximation for optically thick wastes (any waste thicker than 10 to 20 cm), the flux reduces to

$$F_E = \pi I_E = \frac{0.37 \text{CN}_E}{4\kappa_{E,w}} [1 - \exp(-\kappa_{E,w} \rho_w L_w)] \exp(-\kappa_{E,i} \rho_i L_i) \exp(-\kappa_{E,s} \rho_s L_s) \quad (7-6)$$

The length parameters, L_w , L_i , and L_s can be considered as angle-averaged thicknesses of the waste, soil layer, and the steel tube. If the effective surface area of the detector facing the gamma flux is A_d and the intrinsic efficiency (detected fraction of gamma rays that impinge on the detector) is ϵ_E , the count rate P_E is given by

$$P_E = \epsilon_E A_d F_E = \frac{0.37 \epsilon_E A_d C N_E}{4 \kappa_{E,w}} [1 - \exp(-\kappa_{E,w} \rho_w L_w)] \exp(-\kappa_{E,i} \rho_i L_i) \exp(-\kappa_{E,s} \rho_s L_s) \quad (7-7)$$

The effective surface area of the detector is approximately the area of the cylindrical surface of the detector when the detector is surrounded by a cylindrical distribution of waste. The intrinsic efficiency has not been determined for the detector. Based on private communication from J. K. Hartwell, a radiation physicist at the INEEL with many years experience working with gamma detectors, a 40% relative efficiency cylindrical HPGe detector has been used to measure the count rate response from a source in air situated along the centerline at 7 mm from one end (Table 3). The measurement results are presented as the number of gamma rays detected per gamma ray emitted by the source (absolute efficiency). For energies that do not coincide with any gamma spectral line, the number of gamma rays is interpolated from neighboring measurement points. These absolute efficiencies are listed in the table in Appendix A. However, these quantities are not used directly in the formulation of this EDF, which uses the number of gamma rays detected for each gamma ray that hits the detector (intrinsic efficiency). From the measurement data and the geometry of the measurement, the deduced intrinsic efficiency as a function of energy is tabulated below.

Table 3. Intrinsic efficiency of a 40% relative efficiency HPGe detector.

Energy (keV)	Intrinsic efficiency, ϵ_E
100	0.572
200	0.329
300	0.224
400	0.167
500	0.134
600	0.113
700	9.82E-02
800	8.74E-02
900	7.91E-02
1000	7.24E-02

The absolute values of the intrinsic efficiencies of the detector used at Pit 9 are expected to be somewhat smaller than the values given in the above table because of its smaller relative efficiency, but the energy dependency of the efficiency is expected to be very close to the one represented by the values given in the table because, in general, detectors having relative efficiencies in the 20 to 40% range have similar energy dependencies.

A calculation has been performed using the above formula for P_E , assuming that C equals 1 (1 nCi/g) and E equals 414 keV for Pu-239 in a uniform mass of soil around the probe tube. The WMTS calibration (corrected for Pit 9 conditions) gives 68.8 nCi/g for each count per second ($P_E = 1.453 \times 10^2$ c/s for 1 nCi/g). If this value is used as the normalization value, then the factor A_d in the formula for P_E is found to be 164.9 cm², a value not much different from the geometrical surface area of the detector. (A typical 35% cylindrical detector is 57.5 mm in diameter and 61.3 mm long. The total surface area of such a detector is 163 cm².) Note that uncertainties in detector geometry and radiation transport effects are absorbed in the normalization factor for the effective detector surface area.

The formula used to calculate the radionuclide concentrations in the waste based on detector count rate is then given by

$$C\Omega = P_E \left[\frac{0.37 \times 164.9 \epsilon_E N_E}{4\kappa_{E,w}} [1 - \exp(-\kappa_{E,w} \rho_w L_w)] \exp(-\kappa_{E,i} \rho_i L_i) \exp(-\kappa_{E,s} \rho_s L_s) \right]^{-1} \quad (7-8)$$

where C is in nCi/g of matrix material and P_E is the number of counts per second under the photopeak, and ϵ_E is given by the values in the intrinsic efficiency table. An additional factor Ω is introduced into the formula to account for a waste source that subtends a solid angle less than the 2π solid angle as assumed in the earlier derivation and it would also include a reduction factor for the detector surface area when part of the surface area of the detector is not facing the waste. The value of Ω is less than 1 in general and attains the maximum value of 1 for a solid angle 2π radiation seen on any point on the cylindrical surface of the detector. The value $C\Omega$ shall be referred to as the apparent concentration of radionuclides in the waste matrix.

8. MEASUREMENT DATA

The WMTS generated data were transferred to a spreadsheet and the channel numbers of the multi-channel analyzer in the raw data were converted to energy units in keV based on calibration using gamma lines from Pu-239 and Am-241. Over the range between 200 keV and 700 keV, the channel number to energy conversion is very close to linear (0.700 ± 0.008 keV per channel, based on four spectral lines spaced more or less evenly between 200 keV and 662 keV). The channel number to energy conversion was performed with linear interpolation between the calibration points. A typical gamma spectrum is shown in Figure 8-1.

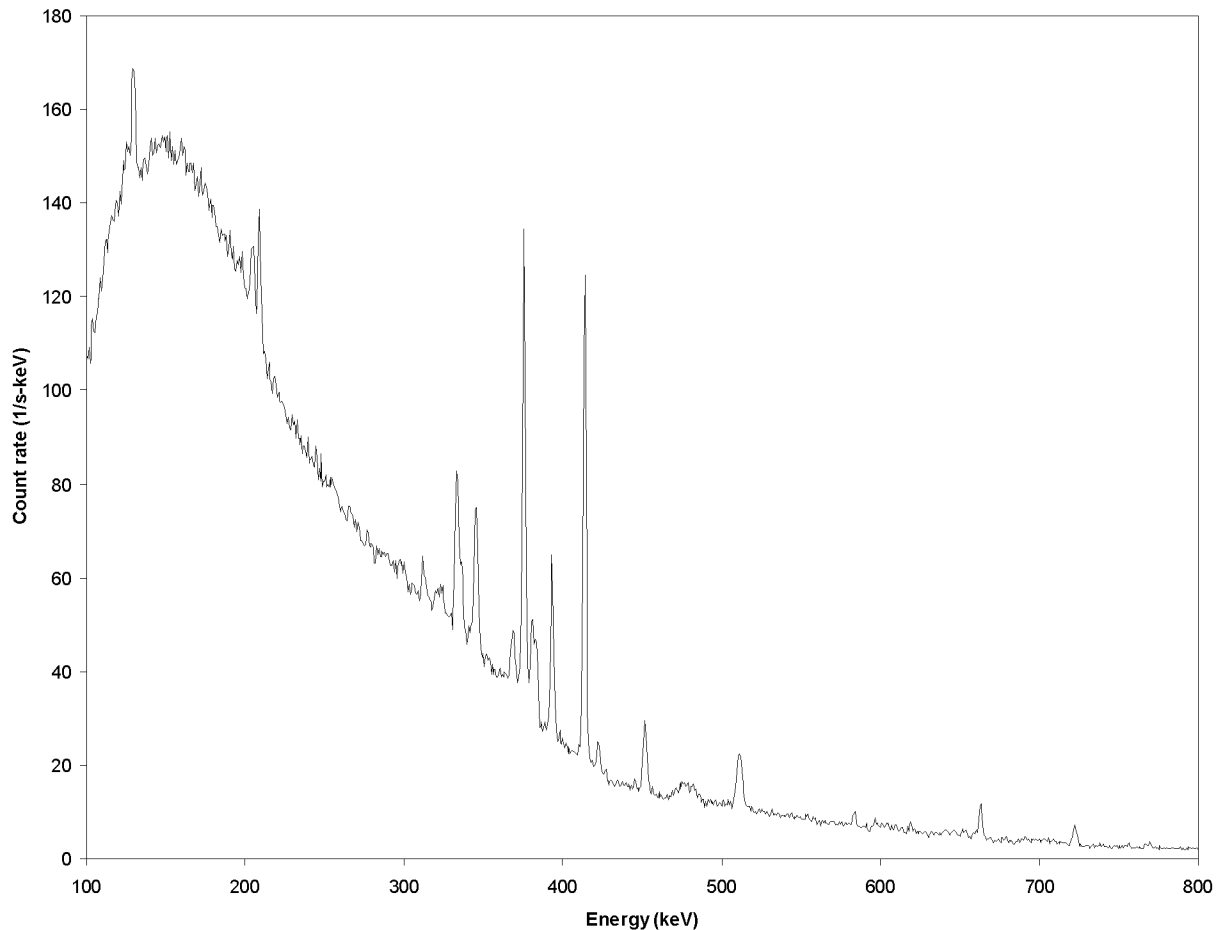


Figure 8-1. Gamma spectrum at the 4.97 ft depth along P9-20.

The count rates under the photopeaks were obtained mostly by integrating (using extended Simpson's rule) the count rates under the photopeaks and subtracting a linear background. Because the 204 keV line of Pu-239 and the 208 keV line of Am-241 are partially resolved, the count rates of these two lines were obtained by fitting two Gaussian profiles; similarly, the count rates of the 375 keV line were obtained by fitting either two or three Gaussians to the partially resolved profiles of the 375 keV, 380 keV, and 383 keV lines of Pu-239. (The 380 keV and the 383 keV lines most of the time appear to be a single, broadened Gaussian.) The count rates, together with their uncertainties of the Pu-239 lines obtained by these methods, are shown in Table 4. For those rates obtained by integration, the uncertainties are based on count statistics, while the uncertainties for the count rates obtained from profile fitting are estimated by visually inspecting the fittings when the parameters are changed.

Table 4. Count rates (counts per second) of P9-20 Pu-239 spectral lines.

Depth (ft)	129 keV	204 keV	345 keV	375 keV	414 keV
4.47	—	—	8.0±1.1	25.4±1.0	26.6±0.94
4.97	—	41±2	82±3.5	244±3.6	269±3.4
5.47	699±26	334±10	413±20	1375±40	1406±21
5.97	858±45	425±30	645±60	1735±70	1787±46
6.47	264±14	220±10	273±10	825±25	893±10
6.97	96±5	48±4	62±2.4	185±7	173±2.3
7.47	77±4	31±2	49±2	150±2	138±1.9

9. LOGGING RESULTS ANALYSIS

One of the objectives of the passive gamma logging effort is to determine the approximate transuranic radionuclide concentrations in the waste buried at Pit 9. In addition to the concentration determinations, it would also be useful from a remediation point of view to ascertain the total amount of transuranic elements. However, for wastes that have dimensions over a few inches, the wastes are generally optically thick to their own radiation in the energy range of interest (100 keV to 1 MeV). Under such a condition, the gamma radiation received at the detector can not be used to deduce the total amount of radionuclides in the waste because the detected radiation carries little information from deep inside the waste matrix. Based on Equation (7-8), only the apparent concentration in the waste can be determined from gamma ray measurements. In addition, in the optically thick limit, the calculated apparent concentration depends only on the mass absorption coefficient of the waste matrix, the optical thickness of a layer of absorbing material between the waste and the detector, the optical thickness of the probe tube, the detector efficiency, and intrinsic properties of the radionuclide.

The apparent concentrations are calculated from the measured count rates for the several gamma rays listed in Table 4. One of the free parameters in Equation (7-8) is the thickness of an inert (soil without radionuclides) absorbing layer. If this thickness is set to zero, which is the case when the waste immediately surrounds the probe tube, the apparent concentrations calculated from the photopeak counts of the several gamma lines generally systematically vary by a large amount, while, theoretically, they should all be the same. This discrepancy (with a systematic energy dependence) in the calculated concentrations from the several gamma lines points to the need to assume that there is a finite layer of soil between the waste and the probe tube. The thickness of this layer is obtained by minimizing the variance of the calculated concentrations from the several gamma lines.

Probe hole P9-20 appears to have unusually high concentrations of Pu-239 from the strengths of its gamma lines. Two waste types, graphite and 743 sludge, are known to potentially contain large concentrations of plutonium. The waste around P9-20 is suspected to be graphite due to the absence of chlorine signatures, which are indicative of 743 sludge. In the apparent concentration calculations, it is assumed that the waste matrix is graphite, with a density of 2 g/cm³ and a thickness of 40 cm. The results depend on the mass absorption coefficient of graphite but are not sensitive to the density and thickness because all the spectral lines are optically thick. Densities of the soil and steel are assumed to be 1.53 g/cm³ and 8.0 g/cm³, respectively.

The results of the calculations based on the measured count rates under the photopeaks are given in Table 5. The standard deviations for the concentrations at various depths refer to the minimum standard deviations of the concentrations calculated from the several gamma lines.

Table 5. Apparent Pu-239 concentrations along P9-20.

Probe Depth (ft)	Average Apparent Concentration CΩ (nCi/g)	Standard Deviation (nCi/g)	Percent Error (std dev/average)	Intervening Soil Layer Thickness (cm)
4.47	3.91E+04	3.83E+02	1.0	21.2
4.97	2.19E+05	5.32E+03	2.4	17.3
5.47	4.45E+05	4.37E+04	9.8	10.8
5.97	6.97E+05	5.88E+04	8.4	11.8
6.47	4.91E+05	1.12E+05	22.8	14.4
6.97	5.46E+04	6.05E+03	11.1	10.2
7.47	4.85E+04	1.60E+03	3.3	11.0

Except for measurement points at 4.47 ft and 4.97 ft, all the spectral lines listed in Table 4 are used to calculate the apparent concentrations. For points at 4.47 ft and 4.97 ft, because the count rates for the 129 keV and the 208 keV lines are indistinguishable from the background, these two lines are excluded from the apparent concentration calculations.

The calculated concentrations at 5.47 ft to 6.47 ft have large errors. Moreover, at these points, the dead time corrections have large, unknown errors, since they range from 70% to 93%, far over the accurate dead time correction limit of 32%.

The apparent concentration versus probe hole depth is plotted in Figure 9-1.

To show the effect of soil absorption on the calculated concentrations from the various gamma lines, the calculated concentrations, with and without soil absorption, are shown in Figure 9-2. Note that the calculated concentrations with soil absorption are more consistent than those calculated without soil absorption. Without assuming soil absorption, the calculated concentrations can be a factor of more than 2 too low at the low energy end than that at the high energy end. In addition, the concentration calculated with soil absorption at 414 keV is approximately a factor 4 over that calculated without soil absorption.

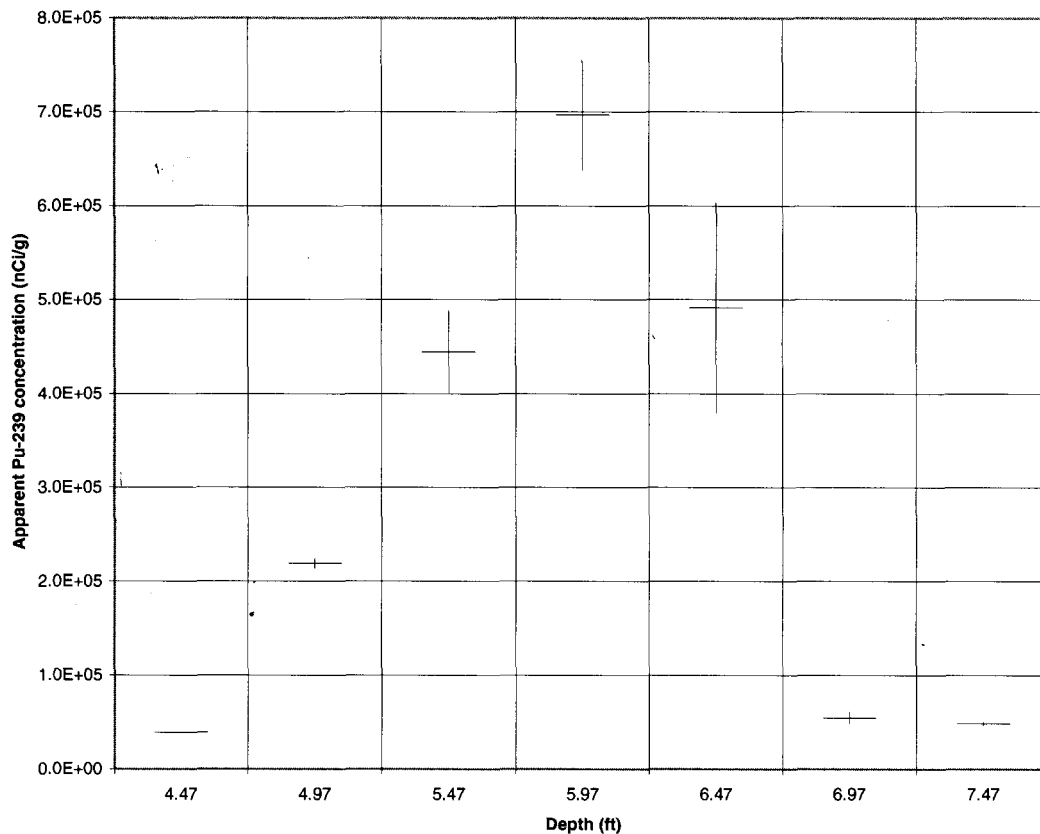


Figure 9-1. Apparent Pu-239 concentrations (C_Ω) along probe hole P9-20.

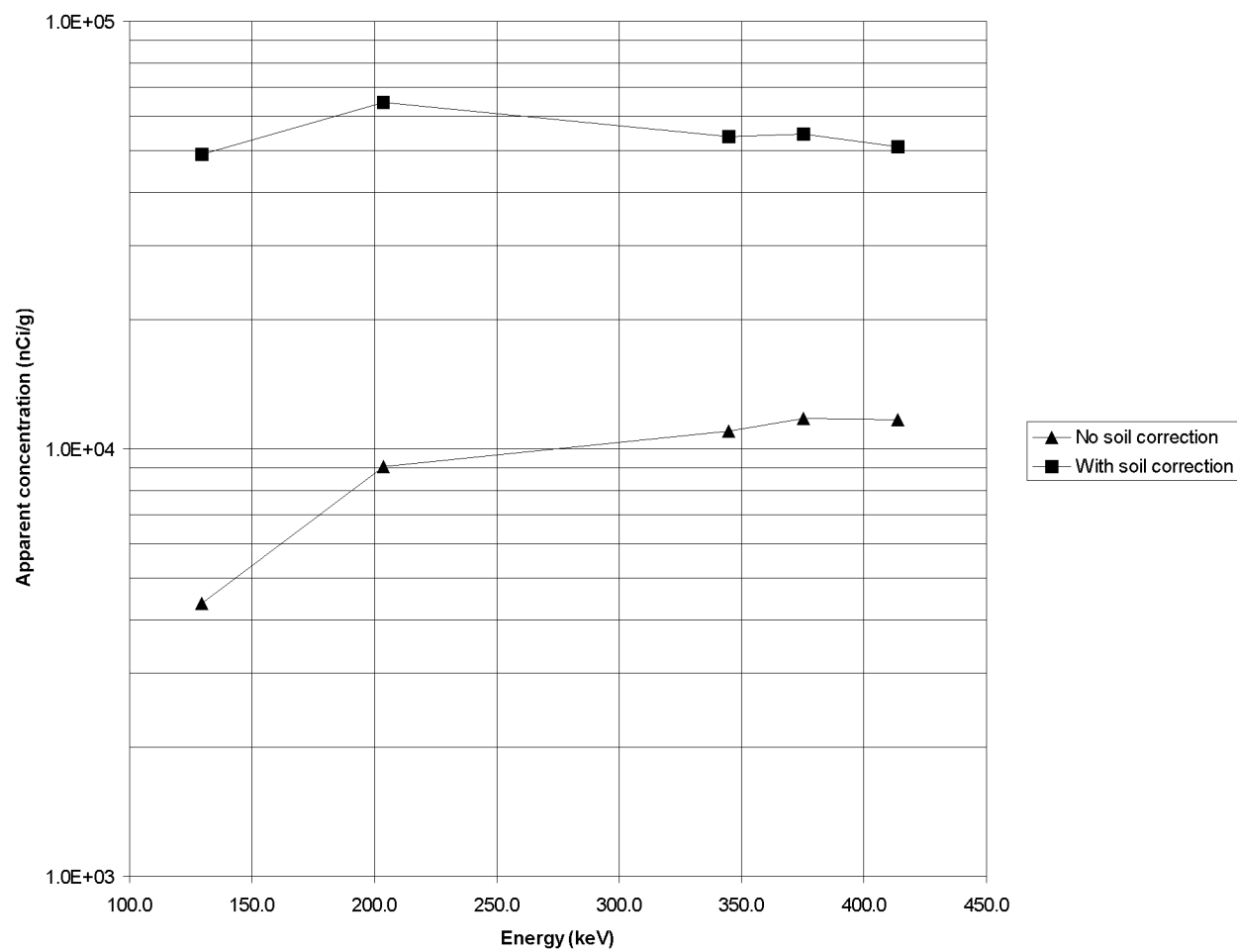


Figure 9-2. Calculated apparent Pu-239 concentrations ($C\Omega$) at the 6.97 ft level.

10. ESTIMATES OF PLUTONIUM-239 CONTENT ALONG PROBE HOLE

The apparent concentration, $C\Omega$, is not a true concentration but rather a concentration weighted by a solid angle subtended by the waste at the detector and by a fraction of the surface area of the detector that faces the waste. The calculation of the apparent concentration, achieved by minimizing the calculated spread from the several spectral lines, indicates a soil layer of approximately 10 cm between the waste and the probe tube. (Part of the soil layer could represent the wall of a drum.) If the waste is confined within a 55-gal drum, as indicated by the vertical extent of approximately 3 ft of the detected radiation, the probe tube would then be offset at some distance from the outer surface of the drum. Consequently, the factor Ω may attain a maximum value of approximately 1/2, because, at most, only half of the detector is facing the waste. This maximum value (1/2) of Ω may be achieved between 4 ft and 6 ft depth where the solid angle subtended by the waste could be a maximum (2π). At these locations, the calculated apparent concentrations are greatest. At other depths, the solid angle would be smaller as the detector moves beyond the ends of the drum. The falloff of the apparent concentrations as the detector moves away from the 6 ft level would indicate that a source is located at approximately 6 ft depth and is off to one side of the probe tube.

To explain the count rates at various depths, a model is constructed to simulate waste located in a single drum. The model has some support in the azimuthal gamma distribution measurements, which show that Pu-239 gamma intensities are skewed high to the south-east quadrant at a depth of 6 ft along P9-20.⁴ (The detector might not have been shielded completely black at azimuthal angles away from an opening to the detector, so radiation was detected at all azimuthal angles. The amount of shielding is unknown, so it can not be firmly established that the waste source was completely off to one side of the probe tube.) The waste is assumed to be graphite (2 g/cm³ density) and has a mass of 100 kg based on disposal records for graphite waste drums disposed of in the area.⁸ To simplify the geometry, it is assumed that the waste is in the form of a sphere. Radiation reaching the detector is assumed to come from a cross-section of the sphere passing through its center and perpendicular to the ray reaching the detector. The geometry of the model is shown in Figure 10-1.

To simplify the integration, it is assumed that the waste sphere is sufficiently far away from the detector so that the radiation can be consider to come from a diametral cross-section of the sphere perpendicular to the γ ray reaching the detector. ("Sufficiently far away" means the radius of the sphere is less than the closest distance from the sphere to the detector.) Furthermore, the solid angle subtended by the source can be approximated by the area of the circular cross-section divided by the square of its distance to the detector. Because the waste sphere is generally optically thick to its own radiation, the count rate of a gamma ray at energy E can be approximated by the following formula:

$$P_E = \frac{0.37\epsilon_E C N_E}{4\pi\kappa_{E,w}} \left(\frac{A_d}{2} \right) \left(\frac{A_s}{r^2} \right) \exp(-\kappa_{E,i}\rho_i L_i) \exp(-\kappa_{E,s}\rho_s L_s) \quad (10-1)$$

All the symbols in Equation (10-1) have the same meaning as those given in Section 7. The new symbols, A_s and r , refer to the waste radiating area (diametral cross-section of sphere) and its distance to the detector, respectively. The effective detector area is approximately $A_d/2$ because radiation comes from only one side of the detector. This may over-estimate the effective area because not all parts of the surface area are parallel to the radiating surface as in the calibration case when the detector is surrounded by a cylindrical source. In fact, when the radiation source is at the level of the detector, the effective area of the detector will be close to the projected cylindrical surface of the detector, i.e., its diameter multiplied by its

height, which is a factor of $\pi/2$ lower than half-cylindrical surface of the detector. This over-estimate of the effective surface area of the detector leads to higher count rates for the same radiation source.

The thickness of the soil layer, L_i , depends on the location of the detector. Referring to Figure 10-1, L_i is given by

$$L_i = [d_s + r_w (1 - \cos \theta)] / \cos \theta \quad (10-2)$$

where d_s is the distance of closest approach of the sphere to the probe tube and r_w is the radius of the waste sphere.

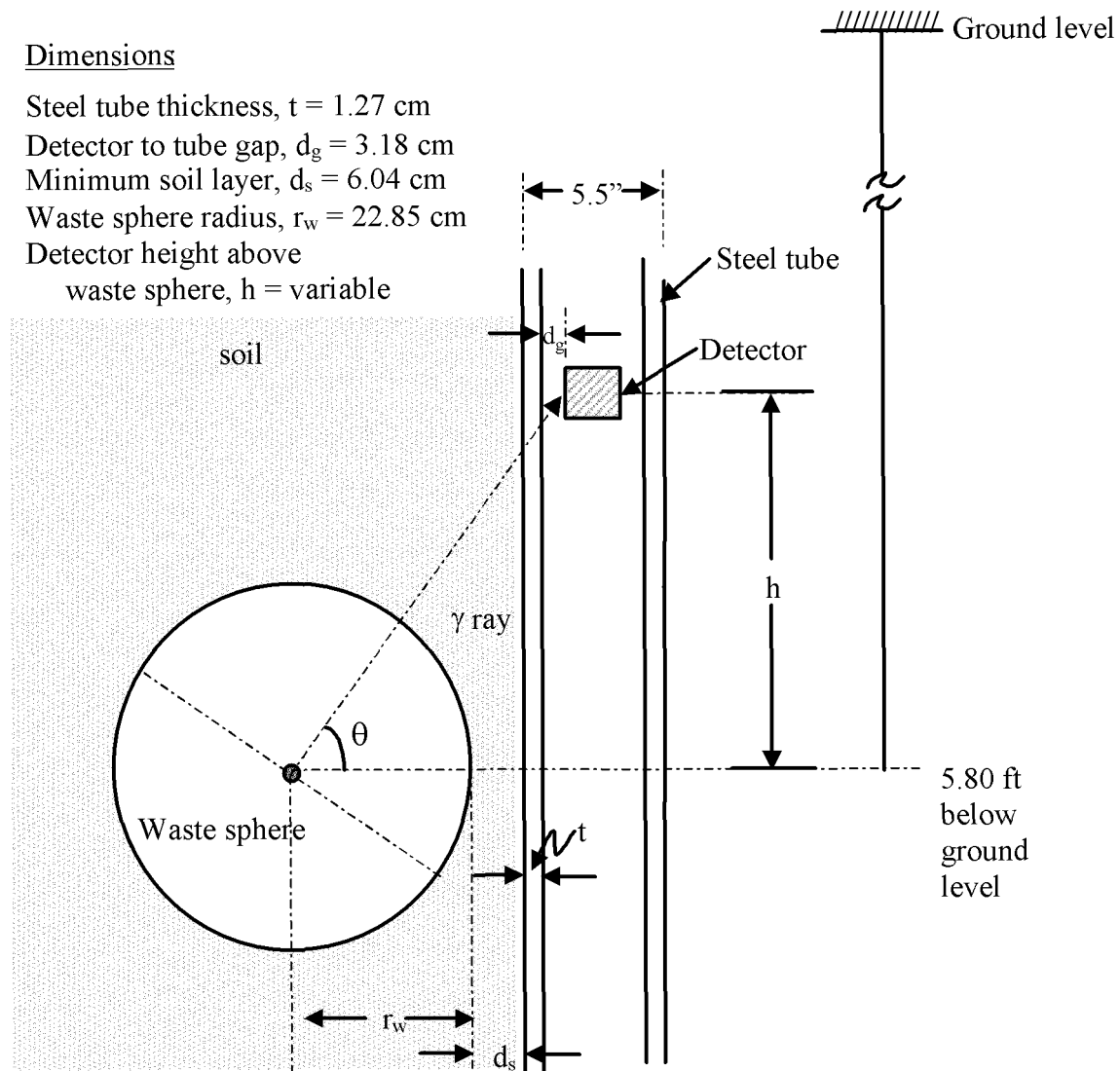


Figure 10-1. Geometry of a localized waste sphere.

The thickness of the steel absorption layer, L_s , also depends on the location of the detector. It is given by

$$L_s = t / \cos \theta \quad (10-3)$$

where t is the thickness of the steel tube.

The angle, θ , is given by

$$\theta = \tan^{-1}(h / (d_g + t + d_s + r_w)) \quad (10-4)$$

where d_g is the gap distance between the detector and the inner surface of the probe tube and h is the vertical displacement of the detector from the center of the waste source.

The numerical parameters given in Figure 10-1 are used to compute the count rates at the various Pu-239 gamma peaks. The Pu-239 concentration that best fits the measurements (minimum sum of squares of differences between measured and predicted values) is 1.35×10^6 nCi/g. At this concentration, the total amount of Pu-239 in the waste sphere is 2170 g.

The total amount of plutonium obtained from the above formulation is not very sensitive to the total mass assumed for the waste for the spherical geometry under consideration. When the total mass is varied, the quantity CAs in Equation (10-1) must be kept constant in order to match the measurements. The total quantity of plutonium is $CV\rho$, where C is its concentration in the waste, V is the waste volume, and ρ is the density of the waste. Assuming that ρ does not vary, then the volume, and hence the mass M , of the waste is proportional to the cube of radius of the waste, or proportional to $As^{3/2}$. Because C is inversely proportional to As , the total quantity of plutonium is then proportional to $As^{1/2}$, or $M^{1/3}$. A 10% error in the waste mass estimate gives only a 3% error in the plutonium mass estimate.

Figures 10-2 through 10-5 show the comparison between the calculated and measured count rates.

It should be noted that because the waste sphere is optically thick, radiation measurements yield no information on the plutonium concentrations in the interior or the back side of the sphere. Consequently, radiation detected from a solid sphere will not be distinguishable from the radiation detected from a spherical shell, as long as the shell is optically thick, nor from the radiation detected from a sphere with the part not facing the detector removed. In these two latter geometries of the waste, the total amount of plutonium will be accordingly reduced.

The comparisons between measured and predicted count rates of the Pu-239 gamma lines are generally good except for locations below the centerline of the hypothetical waste sphere. The disagreements could be due to asymmetrical radionuclide distributions, another minor source in addition to the modeled sphere, or limitations of the simplified model.

To investigate the effect of the size of the sphere on the total amount of estimated plutonium, a model is constructed for a point source with no self absorption. The source is assumed to be located at the center of a hollow sphere having the same diameter as the waste sphere. In order to match the vertical profiles of measured count rates at the various energies, it is found necessary to increase the thickness of the soil absorption layer because self-absorption by the waste is not considered. The closest distance of approach of the sphere (d_s in Figure 10-1) that gives the best match (minimum sum of squares of differences between measured and predicted values) between the measured and predicted profiles is found to be 11.4 cm. The comparisons of fits between measured and predicted count rates are very similar to

those shown in Figures 10-2 through 10-5. The total amount of activity at the center of the sphere is found to be 65.6 Ci, or a Pu-239 mass of 1060 g. (Such an amount of plutonium would greatly attenuate its own radiation, so the estimated total activity is an under-estimate if the measured count rates remain the same. However, if self-absorption is included in the model, the soil absorption layer would have to be reduced, which would counterbalance the effect of plutonium self-absorption on the estimated total amount of plutonium.)

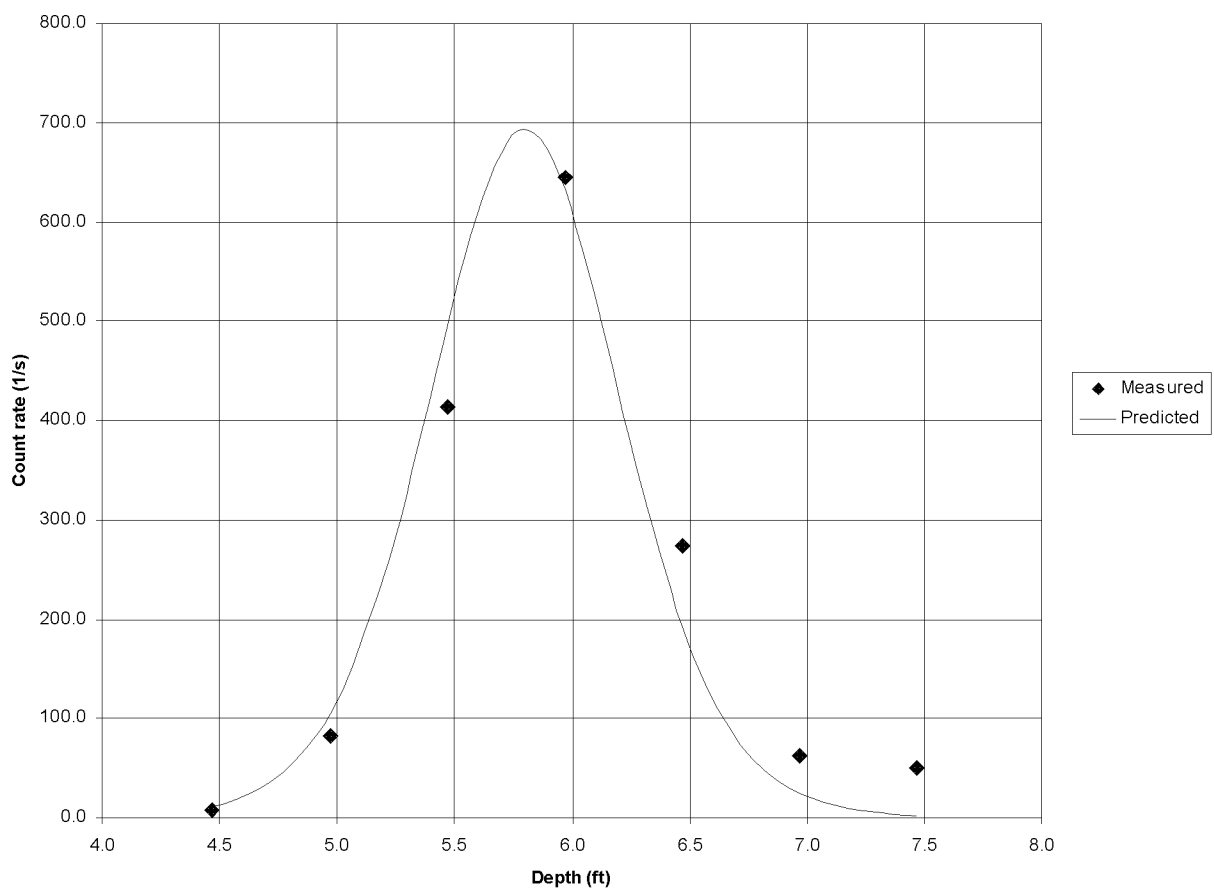


Figure 10-2. Comparison of measured and predicted count rates for Pu-239 204 keV line.

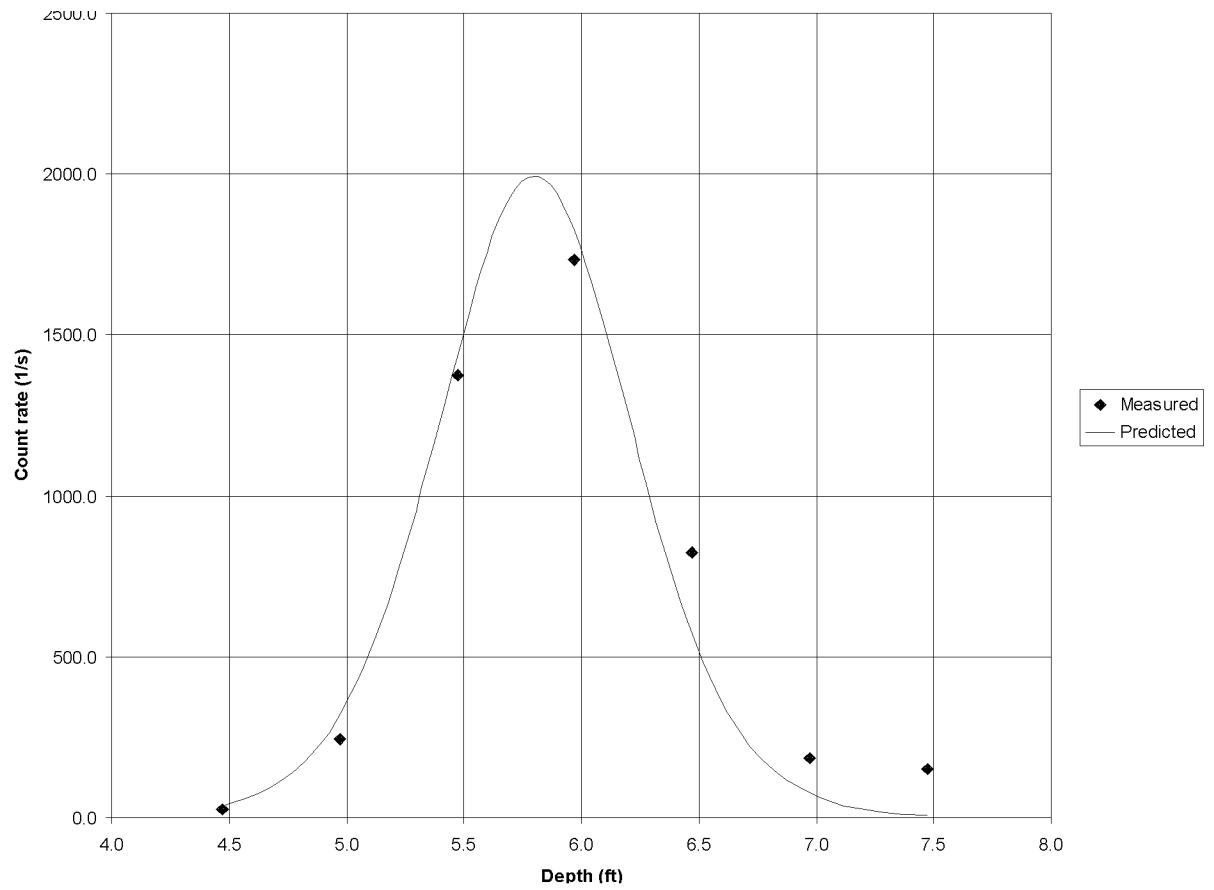


Figure 10-3. Comparison of measured and predicted count rates of Pu-239 345 keV line.

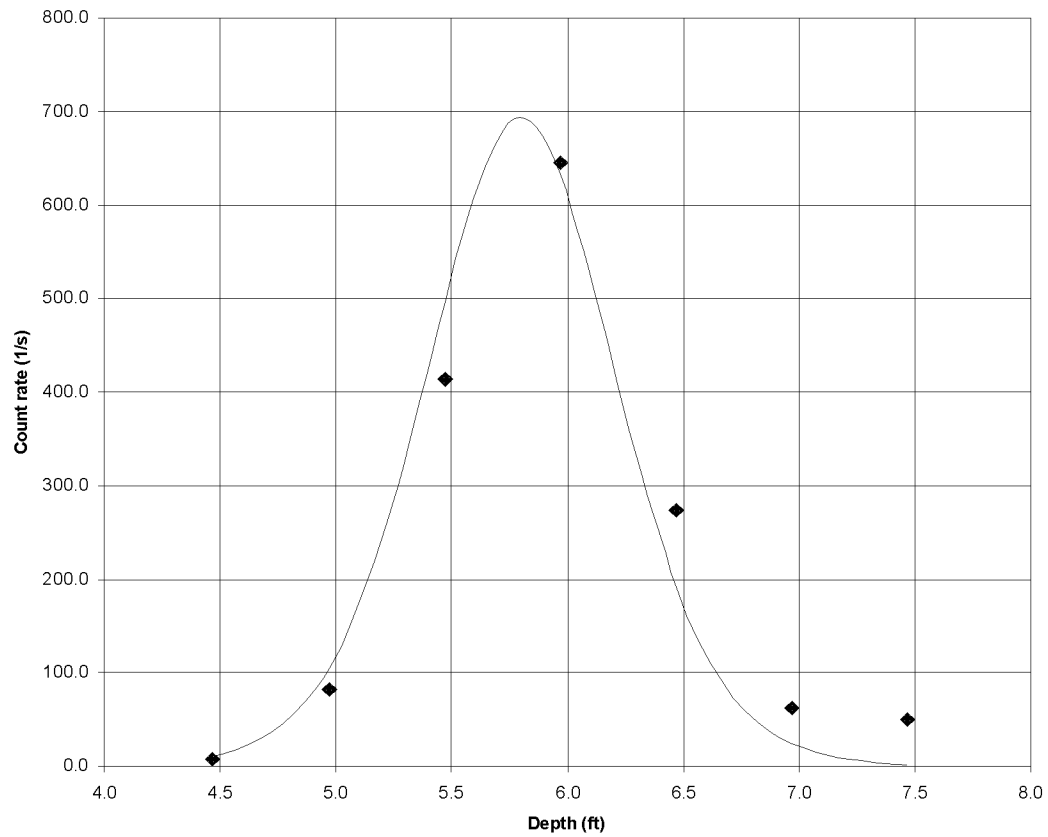


Figure 10-4. Comparison of measured and predicted count rates of Pu-239 375 keV line.

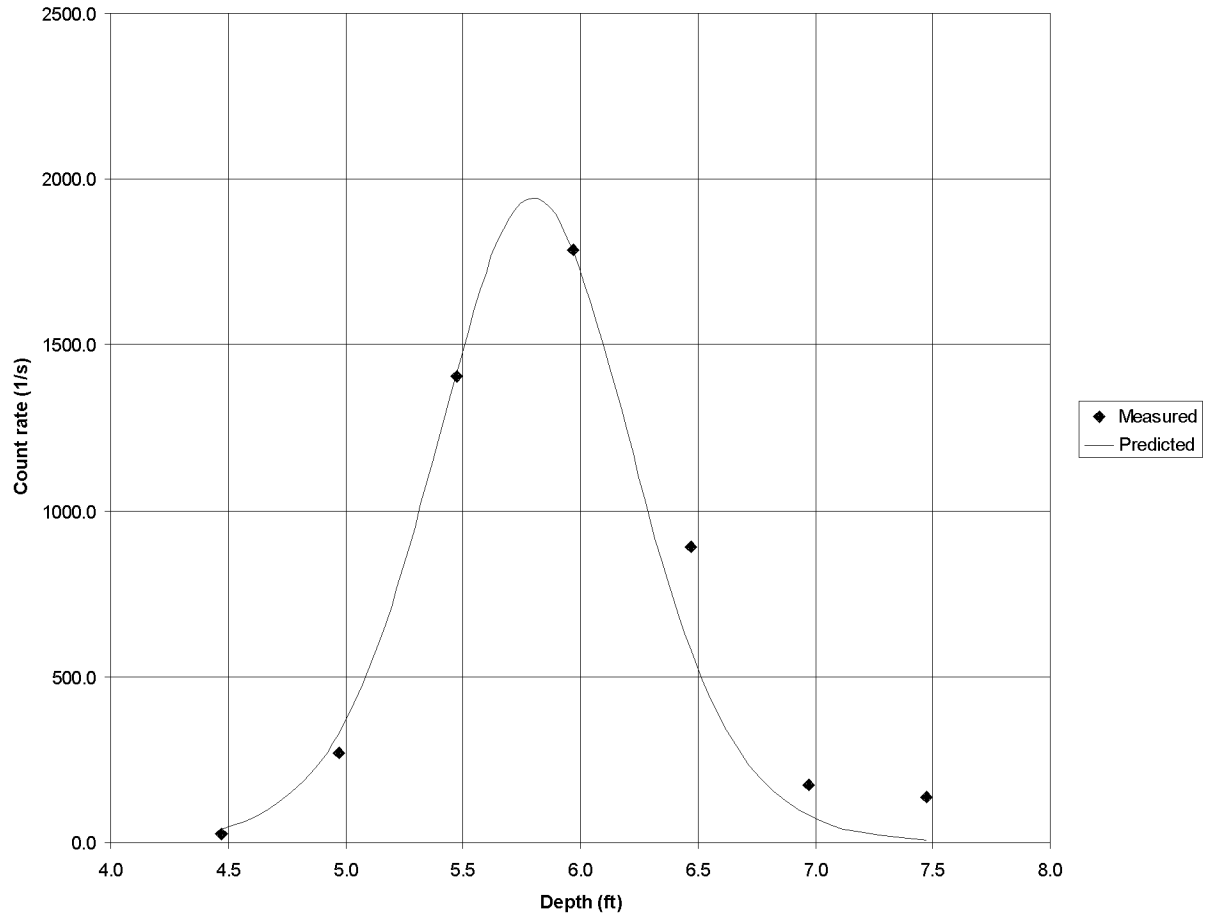


Figure 10-5. Comparison of measured and predicted count rates of Pu-239 414 keV line.

11. DISCUSSION

The modeling results in the previous section indicate that the total amount of plutonium around probe hole P9-20 could be over 1 kg. This section discusses semi-quantitatively the steps used in the analysis to arrive at such an estimate.

The measurements at depths between 5-1/2 ft and 6-1/2 ft have large dead time corrections, which have large, unknown errors, so are the true count rates calculated from the nominal live times. Based on conversations with WMTS personnel and others knowledgeable about the system, it is believed that the system dead time was under-estimated for high count rates, such as those obtained between 5-1/2 ft and 6-1/2 ft. Assuming that the deduced count rates are accurate, based on the WMTS calibration for a cylindrical source surrounding the detector, the Pu-239 concentration at the 6-1/2 ft is over 100,000 nCi/g. If this concentration is applied to a waste of 100 kg mass (waste in a typical graphite waste drum), the Pu-239 content is over 160 g. If the actual dead time correction is higher, the true count rates will be higher and the total amount of plutonium will be proportionally higher.

The first correction made to the WMTS calibration is to include the effect of possible soil absorption. The thickness of the soil layer is determined by using the fact that low energy gamma rays are attenuated more than high energy gamma rays when they go through the same medium. This effect modifies the count rates ratios of these gamma lines from the ratios of their branching ratios in Pu-239 decay. The thickness of the absorbing layer is obtained by adjusting its value in the calculation of the attenuation of the gamma lines until they match the measured line ratios. The minimum thickness of the soil layer is approximately 10 cm when gamma ray measurements at the same depth are considered. At 414 keV, this represents an attenuation factor of 4.3. In other words, the calculated Pu-239 concentration obtained with the WMTS calibration would have to be multiplied by a factor 4.3, or the total amount of Pu-239 would be increased to over 640 g for the same 100 kg of graphite waste.

The second factor applied to the calibration is the reduction in the effective area of the detector that intersects the gamma rays from the waste. If the waste is situated to one side of the detector rather than surrounding the detector, the reduction factor is on the order of 1/2 (a factor of $1/\pi$ is probably more appropriate) if the waste fills one half space and less than 1/2 if the waste is localized, such as waste in a drum. If the reduction factor of 1/2 is applied to the calibration, the Pu-239 amount would be increased by another factor of 2 to over 1,280 g. For effective reduction factors of less than 1/2, the Pu-239 amount would be increased more than a factor of 2.

The third factor applied to the calibration is the reduction of the solid angle subtended by the waste at the detector from 2π to something less. This reduces the fraction of radiation emanating from the waste that reaches the detector. For a waste sphere with a radius of 23 cm (100 kg of graphite) spaced 6 cm (distance of closest approach) from the probe tube, as in the model presented in Section 10, the minimum solid angle reduction factor is approximately 0.4. When this factor is applied to the calibration, the total amount of Pu-239 would be increased from over 1280 g to over 3200 g. This amount is somewhat over the amount of Pu-239 obtained in the spherical graphite waste model presented in Section 10. The discrepancy comes from the approximate nature of the semi-quantitative estimates of the correction factors discussed here.

The biggest factor in increasing the estimated Pu-239 concentrations in the waste matrix comes from correcting for soil absorption. This factor depends on the intrinsic efficiency of the detector as a function of energy as well as on the accuracy of the measurements. Even without this correction factor of 4.3, the total amount of Pu-239 would still be over 500 g.

The applicability of the geometrical model of the waste depends on how well the predicted count rates at a particular energy can fit the measured count rate profile along the vertical positions of the probe hole. It is conceivable that wastes of varying concentrations are distributed uniformly around the probe hole so that they could reproduce the measured count rates with position. In fact, based on the limited number of measurement points, the waste distribution around the probe hole can not be uniquely determined. A discussion of the uniqueness problem is given in Appendix B.

When the waste is optically thick to its own radiation, the total amount of the radioactive source can not be determined by simply measuring the radiation emerging from the waste because the extent of the waste can not be determined. Based on the point source model discussed in Section 10, which does not include the effect of self-absorption, the total amount of plutonium that would fit the measured vertical count rate profile is approximately 1,000 g. This total amount could be lowered further if multiple point sources, or multiple cylindrical sheet sources, around the probe hole are assumed.

12. CONCLUSION

When correction factors are applied to the WMTS calibration of converting gamma ray counts rates into radionuclide concentrations for a waste source that mimics waste contained in a 55-gal drum, the true concentration of Pu-239 in the waste next to the P9-20 probe hole could be over 1,300,000 nCi/g. When this concentration is applied to a waste mass of 100 kg, the total amount of Pu-239 in that waste is over 2000 g. The correction factors applied to the calibration are fairly straightforward and they all correct the concentration upwards from that obtained from the WMTS calibration. These factors correct for soil absorption, loss of detector efficiency because of non-symmetric source around the detector, and geometric dilution because of the finite size of the waste. Although the calculations predicting the count rates to match the measurement are used to obtain the precise correction factors for assumed geometries, these factors can be estimated without elaborate calculations. If the measurements are good and if the WMTS calibration is approximately correct, the model presented in this EDF indicates over 2 kg of Pu-239 near the P9-20 probe hole. However, the estimated quantity of plutonium depends on waste geometry, which can not be uniquely determined, given the limited number of measurement points. For certain waste configurations, e.g., uniform distribution around the probe tube, the measurements are also consistent with plutonium quantities on the order of 100 g.

13. EPILOG

A preliminary draft of the report was circulated in October 2000 among members of the INEEL technical staff and cognizant technical managers of the OU 7-10 Staged Interim Action Project. Upon reviewing the draft, these engineers and scientists recognized the significance of the potential presence of kilogram-quantities of Pu-239 around probe hole P9-20, particularly relating to operational and environmental concerns. Subsequent to their review, radiation physicists within the Nuclear and Radiological Sciences Department at INEEL were requested to review the draft report and, at their discretion, to provide their own estimates of the amount of Pu-239 around probe hole P9-20.

One cursory estimate, made by Dr. J. W. Mandler, an eminent scientist with over 20 years working experience at the INEEL in nuclear radiation measurements, produced a Pu-239 amount on the order 1 kg around probe hole P9-20. Another independent estimate, using a three dimensional point kernel code, RESPMATS, together with detector efficiency normalization to the WMTS calibration, yielded a plutonium mass of 1.7 kg at the 5.5-ft depth and another plutonium mass of 0.8 kg at the 7.5-ft depth, with a total of 2.5 kg of Pu-239 around P9-20. This latter estimate is documented in Appendix C.

A Monte-Carlo calculation, using the same waste sphere geometry documented in Section 10 of this EDF, was performed to predict the response of a typical 35% HPGe detector to a uniform concentration of 1.35×10^6 nCi/g of Pu-239 in the waste sphere (the same concentration used in Section 10 to calculate the count rates) to independently check the results presented in Section 10. The results of this Monte-Carlo calculation are documented in Appendix D. The Monte-Carlo detector count rate results and the results in Section 10 are within a few percent of each other at detector positions more than one waste sphere radius above and below the waste sphere. For detector positions closer to the waste sphere, the Monte-Carlo calculation gives count rates approximately 30% lower than those calculated in Section 10, where the estimates of the effective detector surface area tend to over-estimate the count rate when the detector is close to the waste sphere. (Note that in order to reproduce the count rate near the 5 ft depth level, the concentration of plutonium in the waste sphere assumed in the Monte-Carlo calculation has to increase by approximately 40%, yielding a total plutonium mass of close to 3 kg.) A noteworthy feature of the Monte-Carlo calculation is its modeling of the detector, which provides estimates of the detector efficiency, independent of the WMTS calibrations.

Although the calculation in this EDF (and its verification with a Monte-Carlo calculation) and independent estimates by others all point to a total plutonium mass on the order of kilograms, their validity all depends on a particular conception of a localized distribution of plutonium. As discussed in Section 11 and in Appendix B, the limited number of measurements can not determine unequivocally the geometry of the waste, nor the detailed distribution of plutonium in the waste. Consequently, all estimates presented here can not be considered definitive.

If we assume that the estimated quantities of Pu-239 was indeed buried around P9-20 in a drum, it is interesting to compare those quantities to quantities found in aboveground waste drums from Rocky Flats. Statistical analysis of assay measurements of aboveground waste drums indicates that the probability of finding 1 kg of plutonium in a waste drum is less than one in a few hundred thousand.² To hit such a source in twenty probes into Pit 9 would seem truly serendipitous, if the wastes stored aboveground are representative of what was disposed of in Pit 9.

Based on the significance of a potentially large and localized amount of plutonium under Pit 9, as recognized by technical and managerial personnel, the author would like to see that his estimates of its quantity around P9-20 be verified or dismissed. Further development of the methodology presented in Appendix B could help the planning of future logging efforts in terms of detector design and probe and measurement locations. However, in the absence of recovery and assay of representative materials, further

logging results can improve the estimate of, but may not ascertain, the actual quantities of plutonium around probe hole P9-20.

14. REFERENCES

1. Thomas, R. W., letter to D. E. Wilkins, *Waste Contents Associated with OU 7-10 Stages I/II Activities in Pit 9*, RWT-01-99, April 16, 1999, Lockheed Martin Idaho Technologies Company.
2. Kuan, P., *Probability Distributions of Plutonium and Am-241 in Waste Drums Stored at the Radioactive Waste Management Complex*, EDF-ER-177 (INEEL/EXT-2000-00525), August, 2000, Bechtel BWXT Idaho, LLC.
3. Josten, N., *OU 7-10 Initial Probing Campaign Downhole Logging Results*, EDF-ER-207, September 2000, Bechtel BWXT Idaho, LLC.
4. Kos, S. E., R. K. Price, and R. R. Randall, *Geophysical Logging at Pit 9, INEEL*, Waste Management Technical Services (WMTS), August 2000.
5. Lide, D. R., editor-in-chief, *Handbook of Chemistry and Physics*, 77th Edition, 1996-1997, CRC Press, pp. 10-251 to 10-254.
6. Chu, S. Y. F., L. P. Ekström, and R. B. Firestone, *WWW Table of Radioactive Isotopes, the Lund/LBNL Nuclear Data Search* at the Lawrence Berkeley National Laboratory website, isotopes.lbl.gov/isotopes, Version 2, February 1999.
7. Chandrasekhar, S. *Radiative Transfer*, 1960.
8. Beitel, G. A., P. Kuan, C. W. Bishop, and N. E. Josten, *Evaluation of Stage I Soil Moisture Reading*, INEEL/EXT-2000-00651, October 2000, Bechtel BWXT Idaho, LLC.

Appendix A

Absolute Efficiencies of a 40% HPGe Detector

Appendix A

Absolute Efficiencies of a 40% HPGe Detector

Private communication from J. K. Hartwell, August 2, 2000

Detector dimensions:

Diameter: 58.8 mm

Length: 71.5 mm

Point radiation source along cylindrical axis at 7 mm from one end-cap.

Energy (keV)	Count per γ emitted
100	0.2195
200	0.1264
300	0.0859
400	0.0641
500	0.0514
600	0.0433
700	0.0377
800	0.0336
900	0.0304
1000	0.0278

Appendix B

**On the Derivation of Waste Distribution from
Passive Gamma Measurements**

Appendix B

On the Derivation of Waste Distribution from Passive Gamma Measurements

Multiple measurements of gamma spectra at a number of spatial positions can yield information on the waste distribution around the measurement positions. The efficiency of obtaining that information is facilitated by the presence of multiple gamma lines, separated in energy, from a single radionuclide decay with known intrinsic branching ratios. However, because the number of measurements is limited and the measurements interact in the sense that a discrete source can contribute to measurements at all positions, the solution of the waste distribution problem is not unique based on the measurements. This non-uniqueness is discussed here in conjunction with a formulation of a solution to the problem.

We use tensor notation in the following formulation, i.e., summation over repeated indices in a term is assumed.

We consider a detector placed along a line at positions labeled by subscript index i . The gamma rays from a single radionuclide are labeled by subscript j . First, we consider cylindrical symmetry around the detector, divide the space into radial and axial zones, and label the radiation sources in these zones by $S_{k\ell}$. Without loss of generality, the subscript k will indicate a radial position and the subscript ℓ will indicate a position parallel to the symmetry axis. The indices take on values from 1 to their maximum values (e.g., j takes on the values $1, 2, 3, \dots, j_{\max}$).

Each radiation source contributes a certain amount of counted gamma rays to measurement m_{ij} , the measurement of the j th gamma ray at detector position i . The specific contribution per unit source strength shall be called transfer coefficients (or detector response coefficients) and labeled as $C_{ijk\ell}$, so the total contribution from source $k\ell$ to m_{ij} is $C_{ijk\ell}S_{k\ell}$, i.e.,

$$C_{ijk\ell}S_{k\ell} = m_{ij} \quad (1)$$

The above set of equations has a unique solution if $k_{\max} \times \ell_{\max} = i_{\max} \times j_{\max}$ and the transfer matrix (or detector response matrix) $C_{ijk\ell}$ is non-singular. A necessary condition for non-singularity is that none of the columns or rows of the matrix is zero. Physically this means that no sources beyond a distance that have no effect on the measurements should be included, so the measurements yield no information on such sources. The transfer coefficients can be calculated by analytical or Monte-Carlo methods, or obtained from calibration measurements. To yield meaningful results, the transfer matrix should be such that the solution $S_{k\ell}$ be non-negative.

If the detector positions are spaced far apart such that they do not detect radiation from the same source, the measurements at each level are then separable from each other. The set of equations can then be simplified to

$$C_{jk}S_k = m_j \quad (2)$$

If there are j_{\max} gamma rays, the radial space around the detector can be divided into the same number of regions, each of which contains a source. The higher the number of gamma rays, the better the spatial resolution of the source distribution can be determined. If the gamma rays are spaced far apart in energy such that the transfer coefficients differ from each other by large amounts, then the solution of the distribution will be less sensitive to changes in the measurements.

Under cylindrical symmetry of the detector, the measurements can not distinguish a source on one side of the detector from another source along the circle (or cylindrical surface) at the same radial distance from the detector. The transfer coefficients, however, depend on source geometry. (For non-vanishingly small source zones, the coefficients also depend on the detailed distribution of radionuclides within the zones, e.g., sources distributed as chunks of plutonium will give transfer coefficients different from those given by sources of uniform plutonium distribution.) In general, the transfer coefficients are larger for a source distributed along a larger fraction of the circle than for a source that has a smaller azimuthal extent. The source strength in general varies inversely with the transfer coefficient. In other words, it requires a stronger point source (in terms of total activity) than a cylindrical source to produce the same measurement. In order to break the symmetry of the detector, a shield must be installed around the detector, leaving only a small window that allows radiation to come through. The narrower the window and the thicker the shield, the less ambiguity will result in the source distribution determination.

When measurements at different levels interact, the assignment of source locations will be ambiguous because of the two-dimensional nature of the problem. The number of radial regions can be increased or decreased as long as the number of regions in the axial direction is decreased or increased accordingly so that the total number of regions is kept the same to achieve a solution. To obtain meaningful solutions of the distribution, the assignment of the regions would require experience and good understanding of the radiation transfer process. Devising a methodical assignment of such regions is beyond the scope of this appendix. (Similar remarks apply to measurements at different azimuthal angles.)

Appendix C
Comments and Independent Estimates of
Plutonium Content Around P9-20

Appendix C

Comments and Independent Estimates of Plutonium Content Around P9-20

Y. D. Harker

Subject: Review of EDF-ER-227

Attached is an EXCEL file (and summarized below) with the results of my independent verification the calculations in EDF-ER-227. My approach was to use a three dimensional point kernel code, called RESPMATS, which the INEEL developed for analyzing gamma data from the assay of waste drums. (The draft of a report which describes this method and presents results in analyzing RWMC/SWEPP gamma assay data is now out for review.) The code is specifically designed to handle cylindrical sources and waste matrices with detectors located outside the matrix volume. It calculates a response matrix based on prescribed multiple source zones and multiple detectors. Even though this code was designed for cylindrical geometry, I was able to use it to construct a response matrix for the down hole probe configuration.

The use of simplistic models to approximate complex three dimensional problems has a number of problems. Such types of analysis should be used only as a means to provide estimates with which to identify problems early. However, the availability of highly precise three dimensional analyses almost obviates the use of approximate methods, based on one- or two-dimensional approaches. With the current technology and resources available at INEEL, three dimensional models can be set up very easily and the calculations generally require only a few minutes.

The results given below (the attachment to this Appendix) are based on the assumptions that the calibration done by WMTS was correct and that the counting rates used in the EDF were also correct. However, I have serious reservations concerning the WMTS calibration and measurements.

In the attachment, the first page gives the complete response matrix containing sixteen source zones and 25 measurements. Starting with 16 x 25 matrix, I performed an initial regression analysis producing 16 Pu-239 mass values; i.e., one value for each zone. In subsequent regression analyses, I eliminated those source zones where the Pu-239 mass was not statistically different from zero. This process was repeated until only significantly-different-from-zero Pu-239 masses were obtained for all the remaining source zones. The results of the final analysis are given on the third page of the attachment (and summarized below). On the second page of the attachment, there is a check on the calibration of the method. Based on the WMTS calibration (converted to soil), a uniform concentration of 68.8 nCi/g of Pu-239 should yield a count rate of 1 c/s for the 414 keV line. The check shows that my model and detector efficiencies yielded results that are 30% too high. I also found that the relative energy dependence of the detector efficiency as used in the EDF does not seem to fit responses of the WMTS detector, particularly the 129 keV response. As a result, I used the energy response of the RWMC detectors, which seemed to give more consistent results.

As can be seen from summary below, my analysis indicates that there are two hot spots. The most intense hot spot (1705g of Pu-239) is at a nominal depth 5.5 ft at a radial distance of approximately 30cm from the centerline of the hole. The second hot spot (817g of Pu-239) is at a nominal depth of 7.5ft at a radial distance of 40cm from the centerline of the hole. (My analysis does not distinguish whether a hot spot a single source at the depth and radius indicated or a cylindrical ring source.) The results above are based on plutonium sources buried in soil (density = 1.24 g/cc). If the sources are surrounded by material

with a high density, e.g., due to compression of the soil around the access tube or due to a graphite matrix, then these source strength estimates would be too high. That is, higher density in the surrounding material leads to greater absorption per unit distance. Consequently, the count rates given in EDF-ER-227 could be due to less intense sources closer to the detection point. Therefore, the estimates of source strength in this analysis and in EDF-ER-227 are heavily dependent on assumptions concerning material type and density and also energy dependence of detector efficiency. Until these conditions can be specified more accurately, all estimates of source strength must be considered preliminary.

My data confirm the general conclusion of EDF-ER-227.

Yale D. Harker

	Regression Output:	
	Constant	0
	Std Err of Y Est	230.0
	R Squared	0.7540
	No. of Observations	25
	Degrees of Freedom	23
	zone 11 r = 27cm - 37cm z = 75cm - 105cm nom depth = 5.47 ft	zone 13 r = 37cm - 47cm z = 15cm - 45cm nom depth = 7.47ft
	Pu-239 mass (g)	Pu-239 mass (g)
mass (g)	1705	817
std error (g)	151	508
zone volume (cc)	6.03E+04	7.92E+04
Pu-239 density (g/cc)	2.83E-02	1.03E-02
zone matrix mass (g)	7.50E+04	9.84E+04
zone conc (nCi/g)	1.41E+06	5.16E+05

(a) z= 0 cm corresponds to a depth = 8.47ft

Pit 9 P-920 Analysis

Meas. No.	Depth	Energy	Zone 11 r = 27cm - 37cm z = 75cm - 105cm	Zone 13 r = 37cm - 47cm z = 15cm - 45cm	Meas count rate	Calc count rate
1	7.47 ft	129 keV	0.001323	0.09524	77	80
2	7.47 ft	204 keV	0.001147	0.04902	31	42
3	7.47 ft	345 keV	0.001813	0.05782	49	50
4	7.47 ft	414 keV	0.01247	0.2765	138	247
5	6.97ft	129 keV	0.01436	0.06495	96	78
6	6.97ft	204 keV	0.008446	0.03493	48	43
7	6.97ft	345 keV	0.01085	0.04226	62	53
8	6.97ft	414 keV	0.05809	0.2088	173	270
9	6.47ft	129 keV	0.1159	0.02034	264	214
10	6.47ft	204 keV	0.05001	0.01282	220	96
11	6.47ft	345 keV	0.05452	0.01694	273	107
12	6.47ft	414 keV	0.2387	0.09338	893	483
13	5.97ft	129 keV	0.4725	0.003349	858	808
14	5.97ft	204 keV	0.1712	0.002801	425	294
15	5.97ft	345 keV	0.1699	0.004308	645	293
16	5.97ft	414 keV	0.6615	0.02861	1787	1151
17	5.47ft	129 keV	0.7394	0.0003727	699	1261
18	5.47ft	204 keV	0.2573	0.0004521	334	439
19	5.47ft	345 keV	0.2494	0.0008487	413	426
20	5.47ft	414 keV	0.9411	0.007173	1406	1610
22	4.97ft	204 keV	0.00001845	0.01282	41	11
23	4.97ft	345 keV	0.00004673	0.01694	82	14
24	4.97ft	414 keV	0.0005676	0.09338	269	77
27	4.47ft	345 keV	0.0002906	0.04226	8	35
28	4.47ft	414 keV	0.002636	0.2088	26.6	175

	Regression Output: Constant 0 Std Err of Y Est 230.0 R Squared 0.7540 No. of Observations 25 Degrees of Freedom 23	
	zone 11 r = 27cm - 37cm z = 75cm - 105cm nom depth = 5.47 ft	zone 13 r = 37cm - 47cm z = 15cm - 45cm nom depth = 7.47ft
	Pu-239 mass (g)	Pu-239 mass (g)
mass (g)	1705	817
std error (g)	151	508
zone volume (cc)	6.03E+04	7.92E+04
Pu-239 density (g/cc)	2.83E-02	1.03E-02
zone matrix mass (g)	7.50E+04	9.84E+04
zone conc (nCi/g)	1.41E+06	5.16E+05

(a) z= 0 cm corresponds to a depth = 8.47ft

Appendix D
Monte Carlo Calculation for a Specific P9-20
Waste Geometry

Appendix D

Monte Carlo Calculation for a Specific P9-20 Waste Geometry

W. Y. Yoon

A Monte Carlo calculation was made using MCNP (Reference 1) based on the geometry and estimated source term used in EDF-ER-227. The geometry used is identical to that shown in Figure 10-1 of EDF-ER-227. The source term was assumed to be a spherical mass of graphite with a mass of 100 kg, containing a total inventory of 2170 g Pu-239 (135 Ci). The MCNP program calculated the count rate in counts per second that would be measured in a 35% efficiency HPGe detector 57.5 mm dia. × 61.3 mm long.

The calculated count rates as a function of depth for the four photo peaks (204, 345, 375, and 414 keV) are shown in the table below. These calculated count rates were then compared to the measured count rates shown in Table 4 of EDF-ER-227. This analysis concluded that the source term (estimated in EDF-ER-227) of 2170 grams for the assumed configuration is approximately 30% too low.

Table D-1. Count rates from four principal photo peaks of Pu-239 calculated as a function of depth using MCNP.

Depth (ft)	204 keV	345 keV	375 keV	414 keV
4.47	3.44 ± 0.22	9.66 ± 0.37	30.27 ± 1.09	34.51 ± 1.14
4.97	39.51 ± 1.19	78.04 ± 1.64	238.85 ± 4.78	252.59 ± 4.82
5.47	220.84 ± 7.93	337.71 ± 9.69	986.36 ± 27.62	976.57 ± 26.76
5.80	321.16 ± 9.54	480.74 ± 11.54	1393.61 ± 32.89	1387.76 ± 31.92
5.97	287.06 ± 12.75	441.58 ± 15.68	1308.44 ± 45.01	1233.57 ± 42.43
6.47	77.02 ± 4.68	133.58 ± 6.09	404.15 ± 17.70	422.94 ± 17.76
6.97	8.04 ± 0.34	19.80 ± 0.52	63.41 ± 1.57	66.63 ± 1.57
7.47	0.58 ± 0.046	1.93 ± 0.08	6.95 ± 0.37	7.78 ± 0.38

Reference:

1. "MCNP - A General Monte Carlo N-Particle Transport Code, Version 4B," LA-12625-M, J. F. Briesmeister, Editor, Los Alamos National Lab. (March 1997).

Attachment B

Plutonium Mass Estimation at Type A Probe P9-20 Using Monte Carlo N-Particle Modeling

Woo Yoon

ABSTRACT

This paper describes an attempt to use Monte Carlo N-Particle modeling to determine the amount of plutonium (Pu)-239 mass distributed in the vicinity of probehole P9-20 that is consistent with downhole gamma-ray logging data obtained during November 2000 and June 2001 logging operations. Earlier attempts could not constrained the mass or distribution of plutonium at P9-20. The modeling calculations produced a Pu-239 mass estimate of 407g. An approximate Pu-239 self-shielding correction increases this estimate to a maximum of 490 g.

CONTENTS

ABSTRACT.....	iii
1. INTRODUCTION.....	1
2. BACKGROUND.....	1
3. RELEVANT LOGGING DATA	1
4. ANALYSIS METHOD	3
4.1 MCNP.....	3
4.2 Inverse Modeling Method.....	4
4.3 Volume Subdivision	4
4.4 Assumptions.....	5
5. RESULTS.....	6
5.1 Model 2.....	7
5.2 Self-Shielding Correction	7
6. SUMMARY AND CONCLUSIONS.....	8

FIGURES

1. Location map for P9-20 probe cluster.	9
2. Summary of azimuthal gamma-ray data for P9-20 cluster probes.	10
3. MCNP model subdivision. Note subvolume nomenclature.....	11
4. Plots of measured and MCNP calculated count rates for Model 1 probes.....	12
5. Plots of measured and MCNP calculated count rates for Model 2 probes.....	13
6. 3D visualization of Pu-239 source subvolumes.	14

TABLES

1.	Spectral gamma-ray 414-keV logging data as a function of depth (feet)after conversion to counts/sec (cps).	2
2.	Number of non-zero logging data points for modeled probes.....	5
3.	MCNP model assumptions.	5
4.	Summary of P9-20 MCNP4B model computations.	6
5.	MCNP based mass estimates (in grams Pu-239) for Model 1 subvolumes.	6
6.	MCNP based mass estimates (in grams Pu-239) for Model 2 subvolumes.	7
7.	Macroscopic attributes of MCNP models.....	8

Plutonium Mass Estimation at Type A Probe P9-20 Using Monte Carlo N-Particle Modeling

Woo Yoon

1. INTRODUCTION

This paper describes an attempt to use Monte Carlo N-Particle (MCNP) modeling to determine the amount of plutonium (Pu)-239 mass distributed in the vicinity of probehole P9-20 that is consistent with downhole gamma-ray logging data obtained during November 2000 and June 2001 logging operations. The modeling calculations produced a Pu-239 mass estimate of 407 g. An approximate Pu-239 self-shielding correction increases this estimate to a maximum of 490 g.

2. BACKGROUND

Spectral gamma-ray measurements collected in November 2000 for Type A probehole P9-20 showed a maximum 414-keV gamma-ray count rate of 2,946 counts/sec. The 414-keV gamma-ray is emitted during decay of Pu-239. The P9-20 count rate was nearly three times higher than the highest 414-keV count rate observed elsewhere at the Subsurface Disposal Area.

If Pu-239 is assumed to be uniformly distributed around the probehole, the P9-20 maximum observed count rate would correspond to a Pu-239 activity concentration of 194,000 nCi/g. Depending on the extent of this Pu-239 distribution into the formation surrounding the probehole the total amount of Pu 239 mass associated with P9-20 could be large, raising potential safety concerns. Using only P9-20 logging data, the Pu-239 mass estimate problem is not sufficiently constrained and the total mass estimate is mathematically open ended. Recognizing this shortcoming, the OU 7-10 project directed the collection of additional data to support development of a better Pu-239 mass estimate at P9-20.

Six additional Type A probes were installed and logged in a tight cluster surrounding P9-20 in June 2001. Preliminary review of the June 2001 logging data showed that the high Pu-239 zone observed at P9-20 did not extend outward to the surrounding probes indicating that Pu-239 was localized in the immediate vicinity of P9-20. This result effectively constrained the amount of total Pu-239 mass and substantially reduced safety concerns. However, no formal mass computation was performed.

Plans to excavate soils in the P9-20 area were developed subsequent to the June 2001 logging campaign. To support excavation planning, this formal Pu-239 mass calculation for the P9-20 area based on MCNP simulation code was initiated. This letter report provides a synopsis of the mass calculation effort.

3. RELEVANT LOGGING DATA

Figure 1 shows the location of the November 2000 and June 2001 P9-20 cluster probeholes. Subcontractor delivered spectral gamma-ray data for the cluster probes were used as the basis for modeling. For each probe, 414-keV gamma-ray data were converted to units of counts/sec (Table 1). Of primary interest for the present study are the elevated count rate peaks at 5.5–6.5 ft. The study objective was to develop an estimate of the Pu-239 mass distribution associated with these peaks.

Table 1. Spectral gamma-ray 414-keV logging data as a function of depth (feet)after conversion to counts/sec (cps).

P9-20		P9-20-01		P9-20-02		P9-20-03		P9-20-04		P9-20-05		P9-20-06	
depth (ft)	cps	depth	cps	depth	cps	depth	cps	depth	cps	depth	cps	depth	cps
0.5		0.0		0.0		0.0		0.0		0.0		0.5	
1.0		0.5		0.5		0.5		0.5		0.5		1.0	
1.5		1.0		1.0		1.0		1.0		1.0		1.5	
2.0		1.5		1.5		1.5		1.5		1.5		2.0	
2.5		2.0		2.0		1.5		2.0		2.0		2.5	
3.0		2.5		2.5		2.0		2.5		2.5		3.0	
3.5		3.0		3.0	0.2	2.0		3.0		3.0		3.5	0.3
4.0	2.9	3.5		3.5	2.6	2.5		3.5		3.2		4.0	5.9
4.5	34.5	4.0	4.7	4.0	6.4	3.0		4.0		4.0		4.5	51.1
5.0	362.9	4.5	17.4	4.5	15.1	3.5		4.5		4.5	12.6	5.0	170.7
5.0	382.2	5.0	53.3	5.0	31.9	4.0		5.0	0.1	5.0	44.1	5.5	206.9
5.5	2,081.0	5.5	141.3	5.2	81.8	4.5	2.6	5.5	0.9	5.5	68.0	6.0	176.2
5.5	2,156.8	6.0	622.1	6.0	99.5	5.0	26.6	6.0	1.6	6.0	49.0	6.5	75.5
6.0	2,945.5	6.5	624.7	6.5	62.5	5.5	87.4	6.5	2.3	6.5	40.4	7.0	29.4
6.0	2,939.1	7.0	143.2	7.0	34.2	6.0	88.0	7.0	4.0	7.0	30.1	7.5	9.7
6.5	911.5	7.5	15.1	7.5	46.8	6.0	89.9	7.5	6.7	7.5	5.4	7.7	4.4
6.5	887.8	8.0	6.2	8.0	47.7	6.5	52.7	8.0	5.6	8.0	3.2	8.5	1.9
7.0	283.0	8.5	10.6	8.5	29.3	6.5	54.2	8.5	6.9	8.5	3.5	9.0	1.0
7.0	278.1	9.0	21.6	9.0	19.5	7.0	35.9	9.0	6.0	9.0	2.8	9.5	1.1
7.5	141.0	9.5	8.3	9.5	19.3	7.0	34.8	9.5	7.2	9.5	2.6	10.0	0.7
7.5	142.3	10.0	5.0	10.0	10.3	7.5	13.1	10.0	4.8	10.0	1.9	10.5	
8.0	52.3	10.5	4.2	10.5	2.5	7.5	14.4	10.5	3.3	10.5	0.3	11.0	
8.0	51.4	11.0	0.3	11.0	0.8	8.0	10.8	11.0	1.5	11.0		11.5	
8.5	29.1	11.5		11.5		8.0	11.8	11.5		11.5		11.9	
8.5	28.2	12.0		12.0		8.5	27.8	11.5					
9.0	53.1	12.5		12.2		8.5	27.4	12.0					
9.0	54.3	13.0				9.0	42.1	12.0					
9.3	8.1	13.4				9.0	40.8	12.3					
10.0	10.5					9.5	50.1						
10.5	2.2					9.5	53.6						

Table 1. (continued).

P9-20		P9-20-01		P9-20-02		P9-20-03		P9-20-04		P9-20-05		P9-20-06	
depth (ft)	cps	depth	cps	depth	cps	depth	cps	depth	cps	depth	cps	depth	cps
11.0	0.1					10.0	83.7						
11.5						10.0	85.5						
11.9						10.5	26.7						
						10.5	28.6						
						11.0	2.8						
						11.0	3.6						
						11.5	0.6						
						11.5	0.6						
						11.9	1.2						

Azimuthal gamma-ray logging, a method developed by the OU 7-10 project in conjunction with a downhole logging subcontractor, is used to determine the angular position of a gamma-ray source in the vicinity of a probehole. Azimuthal logging was performed in June 2001 for the P9-20 probe cluster at the 5.5–6.5 ft depth range as shown in Figure 2. The azimuthal data showed that the Pu-239 source at this depth was located primarily to the south of P9-20.

4. ANALYSIS METHOD

The MCNP simulation method was used for Pu-239 mass analysis. MCNP simulation permits the analyst to devise hypothetical Pu-239 mass distributions and to calculate synthetic gamma-ray detector responses for comparison with measured logging data. The following sections give a brief description of the MCNP method as employed for P9-20 modeling.

4.1 MCNP

The MCNP4B¹ code was utilized in the P9-20 source study. MCNP4B is a standard probability-based analysis code for simulating nuclear phenomenon. MCNP codes simulate the production and fate of nuclear particles (or photons) based on known probabilities for nuclear interactions. In the current study, the MCNP code simulated the transport and interaction of Pu-239 414-keV gamma-rays through the soil media, steel probehole casing and HPGe detector. Photo-peak count rates resulting from energy deposition of the 414-keV gamma-ray in the detector crystal were obtained per source photon.

¹ MCNP, 1997, "MCNP - A General Monte Carlo N-Particle Transport Code," Version 4B, LA-12625-M, J. F. Briesmeister, editor, Los Alamos National Lab, March 1997.

4.2 Inverse Modeling Method

The MCNP forward model may be generalized as

$$F(S) = M$$

where S represents a set of discrete Pu-239 source volume elements, F represents the MCNP modeling computation, and M represents the gamma-ray count rates that would be observed by a gamma-ray logging system at a set of predefined measurement points. In the forward model, simulated logging measurements can be produced by assigning Pu-239 concentrations to subsurface volume elements and performing the MCNP calculation.

For P9-20, we have a set of actual logging measurements (M matrix) and seek the set of Pu-239 source volume elements that would produce these measurements, i.e. we must solve the inverse problem

$$F^{-1}(M) = S$$

where the parameter designations are the same as for the forward problem. Computationally, the inverse problem is solved by an iterative process that progressively adjusts the Pu-239 source in each subvolume until the simulated count rates match the actual logging measurements within some prescribed tolerance. Model iteration is performed manually, which means that the analyst manually adjusts the Pu-239 mass distribution and re-runs the MCNP computation at each step. The P9-20 results described in this report were obtained from a single iteration of the MCNP computation.

4.3 Volume Subdivision

Two models were constructed using two sets of three adjacent probeholes as shown in Figure 3. The chosen model volumes correspond with the areas of highest apparent Pu-239 concentration based on azimuthal logging data. The two models, designated as Model No. 1 and Model No. 2, were computed separately and are completely independent of each other, i.e., they provide two alternative solutions to the Pu-239 source distribution problem. The subsurface outside of the model volumes is assumed to contain no Pu-239.

MCNP4B permits the model volume to be subdivided into a number of subvolumes. The number of subvolumes must be equal to the number of measurement points used in the simulation. For each model the measurement points includes all non-zero logging data values between the depth interval from 3.5 to 12.0 ft for each of the three probeholes interior to the model volume. The number of non-zero measurement points for each probe within the stated depth interval is shown in Table 2 as well as the total number of non-zero measurements for the two 3-probe models. Some additional pseudo-measurements were obtained by interpolating the logging data to bring the total number of measurement points for each model to 64.

Table 2. Number of non-zero logging data points for modeled probes.

Probe	Non-Zero Values	Interpolated Values	Total Values
P9-20	24	1	25
P9-20-01	15	4	19
P9-20-06	14	6	20
P9-20-05	13	6	19
Model 1 (P9-20, -01, -06)	53	11	64
Model 2 (P9-20, -05, -06)	51	13	64

Each 3-probe model volume was subdivided into 64 subvolumes, representing 16 six inch thick soil layers between 4 and 12 feet deep. Note that this subdivision scheme results in small subvolumes near P9-20 and larger sub-volumes near adjacent probes.

4.4 Assumptions

The MCNP computation includes the logging tool and measurement environment as part of the subsurface model. These model elements are described in terms of their physical dimensions and/or molecular composition. Table 3 lists the characteristics assumed for the P9-20 MCNP models. Where appropriate, notes provide the basis for specific assumed values.

Table 3. MCNP model assumptions.

Assumed Parameter	Parameter Value	Note
Soil	1.89 g/cm ³ 70% SiO ₂ , 5% H ₂ O, 25% void	Typical idealized unconsolidated soil
Probe casing	1/2-in. thick, steel	Known value
HPGe detector	Cylindrical, germanium 57.5 mm diameter, 61.3 mm long	Ortec recommended value for 35% detector
Detector position	Centered in probehole	Tool employed a centering device
Detector housing	1.54 mm thick, steel	Typical value
Pu-239 distribution	Uniform within each subvolume	

5. RESULTS

Results from the two model computations are summarized in Table 4. A comparison of measured versus MCNP calculated values is shown in Figures 4-5. The MCNP Pu-239 mass estimates associated with each model are shown in Figures 6-7.

Table 4. Summary of P9-20 MCNP4B model computations.

Model	Probes	Computed Pu-239 Mass	Computed Pu-239 Counts/Sec	Measured Pu-239 Counts/Sec	Number of MCNP Iterations
1	P9-20, P9-20-01, P9-20-06	385.8 g	18,569	17,407	1
2	P9-20, P9-20-06, P9-20-05	428.3 g	19,710	15,464	1
	AVERAGE	407.1 g	19,140	16,436	

Each 3-probe model volume was subdivided into 64 subvolumes, representing 16 six-inch thick soil layers between 4 and 12 feet deep. Note that this subdivision scheme results in small subvolumes near P9-20 and larger sub-volumes near adjacent probes.

Table 5. MCNP based mass estimates (in grams Pu-239) for Model 1 subvolumes.

Model 1	1A	1B	1C	1D	2A	2B	2C	2D
Z1 (4-5)	0	0	0	0	0	30	0	0
Z2 (5-6)	9	0	15	0	0	0	0	0
Z3 (6-7)	100	0	0	0	0	0	0	0
Z4 (7-8)	7	0	0	0	0	0	0	0
Z5 (8-9)	1	0	5	0	0	0	33	0
Z6 (9-10)	2	0	0	0	0	0	0	0
Z7 (10-11)	0.2	0	0	34	0	0	0	0
Z8 (11-12)	0	0	0	0	0	9	0	143

Figure 4 log plots show that the Model 1 mass distribution gives an approximate fit for the 414-keV peak between 4–8 ft in P9-20. This fit was obtained by placing 188 g of Pu-239 within six 1A subvolumes immediately adjacent to P9-20 (Table 5, Figure 6a). This compact Pu-239 mass geometry gives the lowest mass solution to the MCNP inverse problem at P9-20. However, the 1A subvolumes do not produce a fit with logging data at 4–8 ft in P9-20-01 and P9-20-06. Furthermore, secondary Pu masses placed in subvolumes 1CZ2 and 2BZ1 were insufficient to match the logged 414-keV count rates in these outer probes so that the overall solution at 4–8 ft in these probeholes is poor.

Subvolumes Z5–Z8 are not relevant to the major 414-keV at 4–8 ft. However, it is worth noting that subvolumes 1DZ7 and 2DZ8, which together encompass 177 g of Pu-239, produce only weak simulated count rates in P9-20-01 and P9-20-06 respectively. The cause-effect comparison between these subvolumes and the 1A subvolumes discussed above illustrates the difference between a compact versus distributed mass.

Overall Model 1 provides a reasonable estimate of the minimum Pu mass associated with the observed 414-keV peak in P9-20. Model 1 depicts a scenario where the 4–8 ft count rate peak in P9-20 is NOT associated with the count rate peaks in the outer probeholes over the same depth range.

5.1 Model 2

Table 6 shows the Pu-239 mass estimates for each subvolume of Model 2 following the subvolume nomenclature of Figure 3.

Figure 5 log plots show that the Model 2 mass distribution also gives an approximate fit for the 414-keV peak between 4–8 ft in P9-20. In this case, the fit was obtained by placing 76 g of Pu-239 within an single 1A subvolume immediately adjacent to P9-20 (Table 6, Figure 6b). As for Model 1, the compact 76 g 1A mass has little effect on count rates in P9-20-06 and P9-20-05, suggesting that elevated 414-keV count rates in these adjacent holes is due to a secondary Pu mass. Model 2 is another example of a minimum Pu-239 mass solution to the P9-20 inverse problem.

Table 6. MCNP based mass estimates (in grams Pu-239) for Model 2 subvolumes.

Model 2	2A	2B	2C	2D	3A	3B	3C	3D
Z1 (4-5)	0	0	0	0	0	0	0	0
Z2 (5-6)	0	0	0	0	5	0	119	0
Z3 (6-7)	76	0	0	0	0	0	0	0
Z4 (7-8)	0	0	0	0	0	37	0	0
Z5 (8-9)	0	0	33	0	0	3	0	0
Z6 (9-10)	0	0	0	0	0	13	0	0
Z7 (10-11)	0	0	0	0	0	0	0	0
Z8 (11-12)	0	0	0	142	0	0	0	0

5.2 Self-Shielding Correction

Due to the high density of Pu-239, significant self-shielding can occur if individual Pu-239 particles exceed about 100 μm in size. Self-shielding would cause gamma-ray attenuation and lower the observed count rates during gamma-ray logging. If we assume that the total Pu-239 mass in each subvolume is composed of uniformly distributed 1000 μm particles, attenuation would be approximately 20% greater than in the assumed case of uniform distribution of sub- μm particles throughout the subvolumes. The net results would be to increase the MCNP mass estimates by 20%.

6. SUMMARY AND CONCLUSIONS

Model 1 and Model 2 produced total Pu-mass estimates of 385.8 g and 428.3 g Pu-239, respectively. These values represent the total Pu-239 mass within the entire model volume. Table 7 summarizes macroscopic characteristics of the two models.

Table 7. Macroscopic attributes of MCNP models.

Attribute	Model 1	Model 2
soil volume(cm ³)	1.95E+06	1.70E+06
soil volume (cu ft)	68.7	60.1
soil mass (g)	3.68E+06	3.22E+06
soil mass(tons)	4.05	3.55
Pu mass (g)	385.8	428.3
Pu activity (nCi)	2.39E+10	2.66E+10
Pu activity concentration (nCi/g)	6,505	8,256

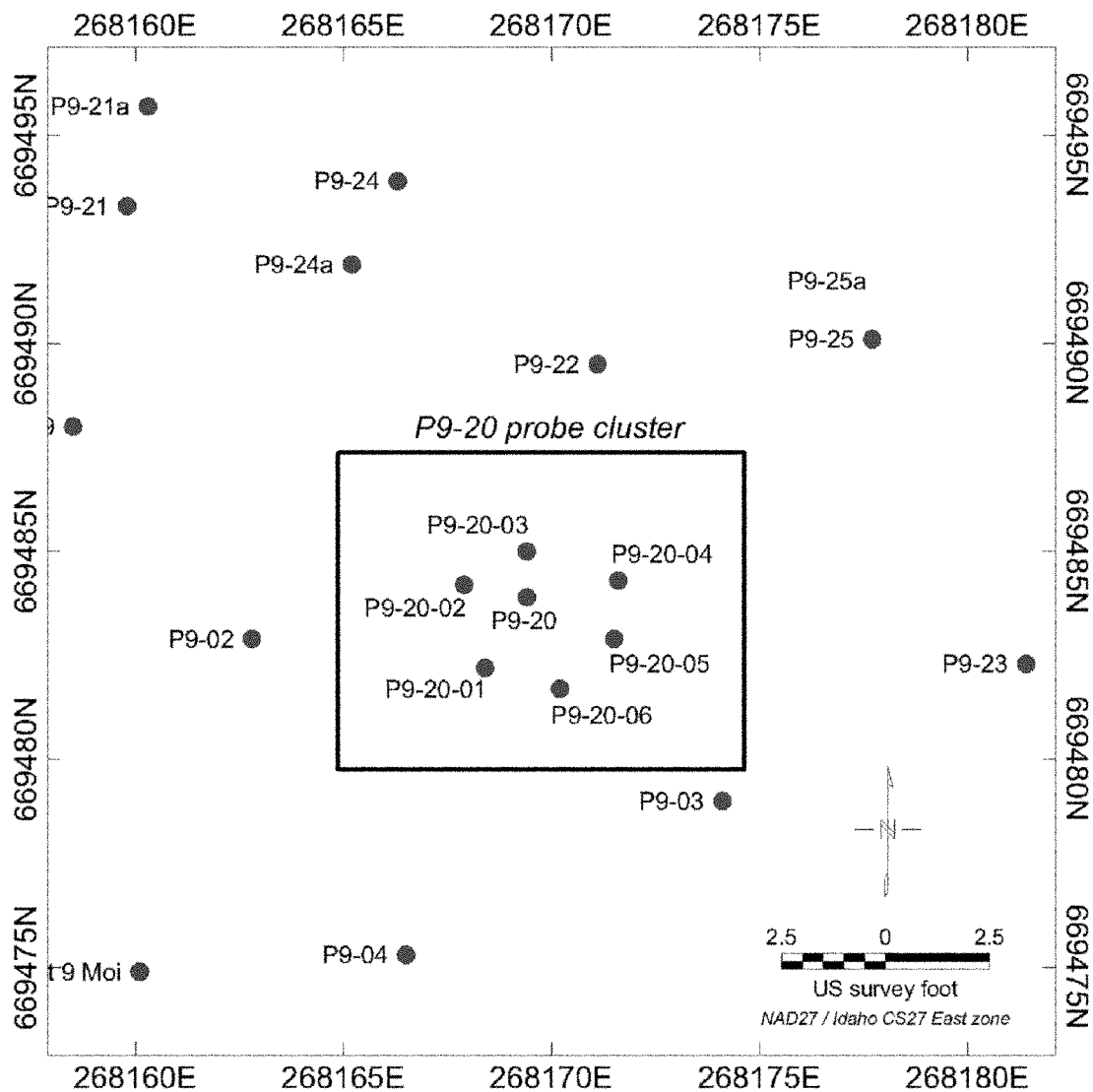


Figure 1. Location map for P9-20 probe cluster.

P9-20 cluster probe summary Pu-239 @ 6.0 ft

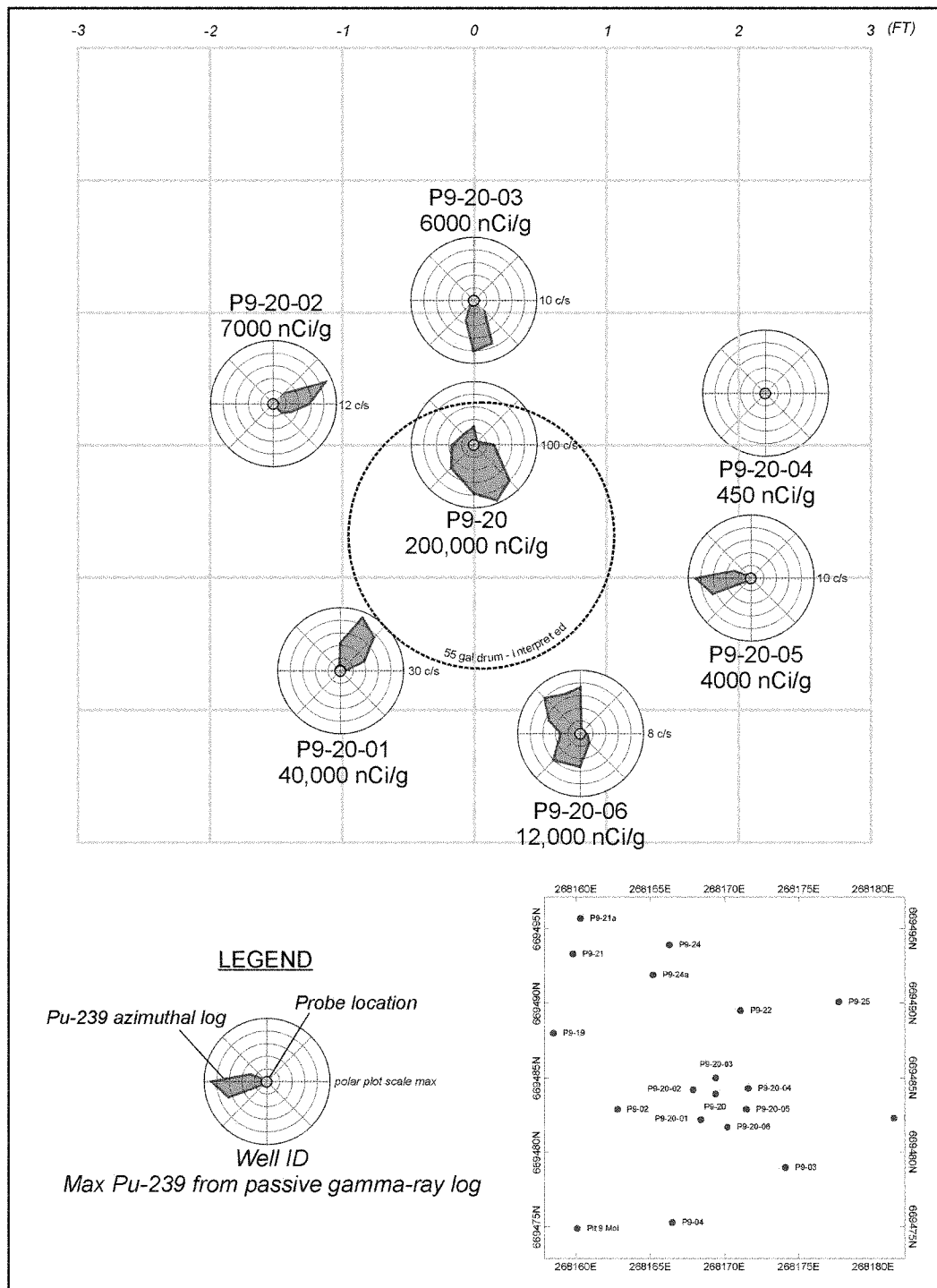
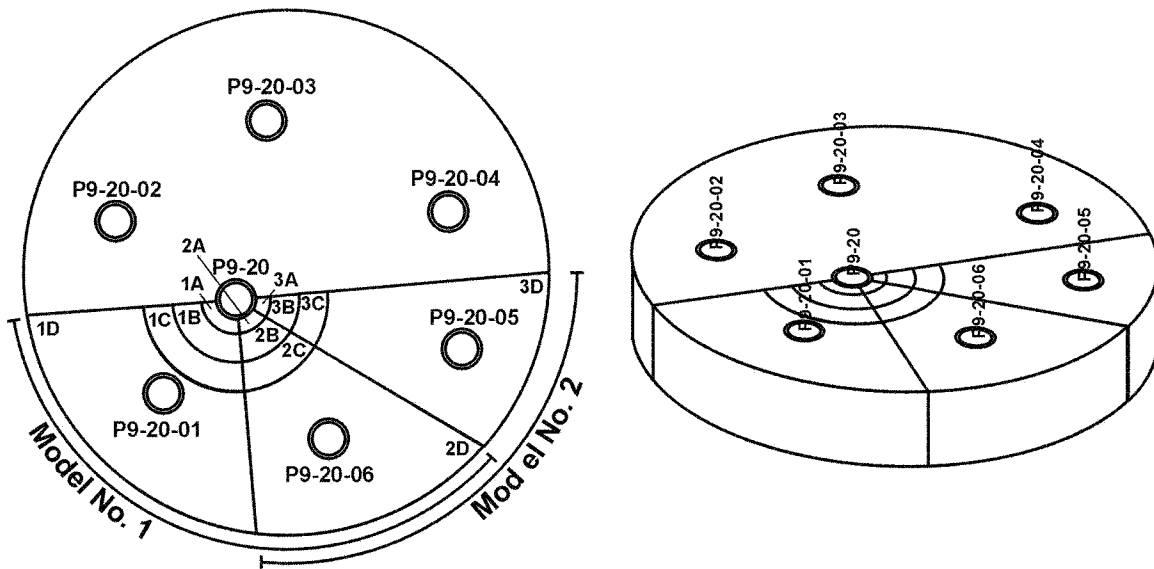
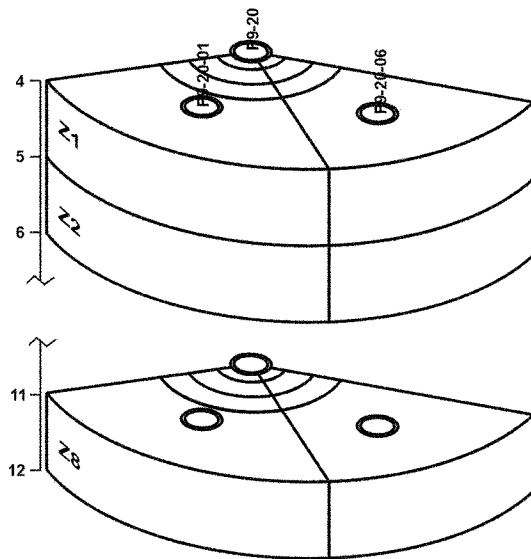


Figure 2. Summary of azimuthal gamma-ray data for P9-20 cluster probes.

P9-20 probe cluster



MCNP Model No. 1



MCNP Model No. 2

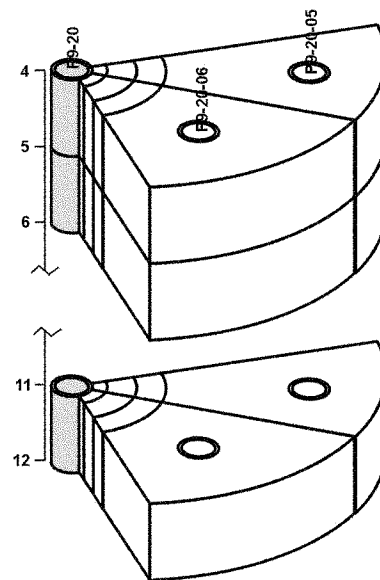


Figure 3. MCNP model subdivision. Note subvolume nomenclature.

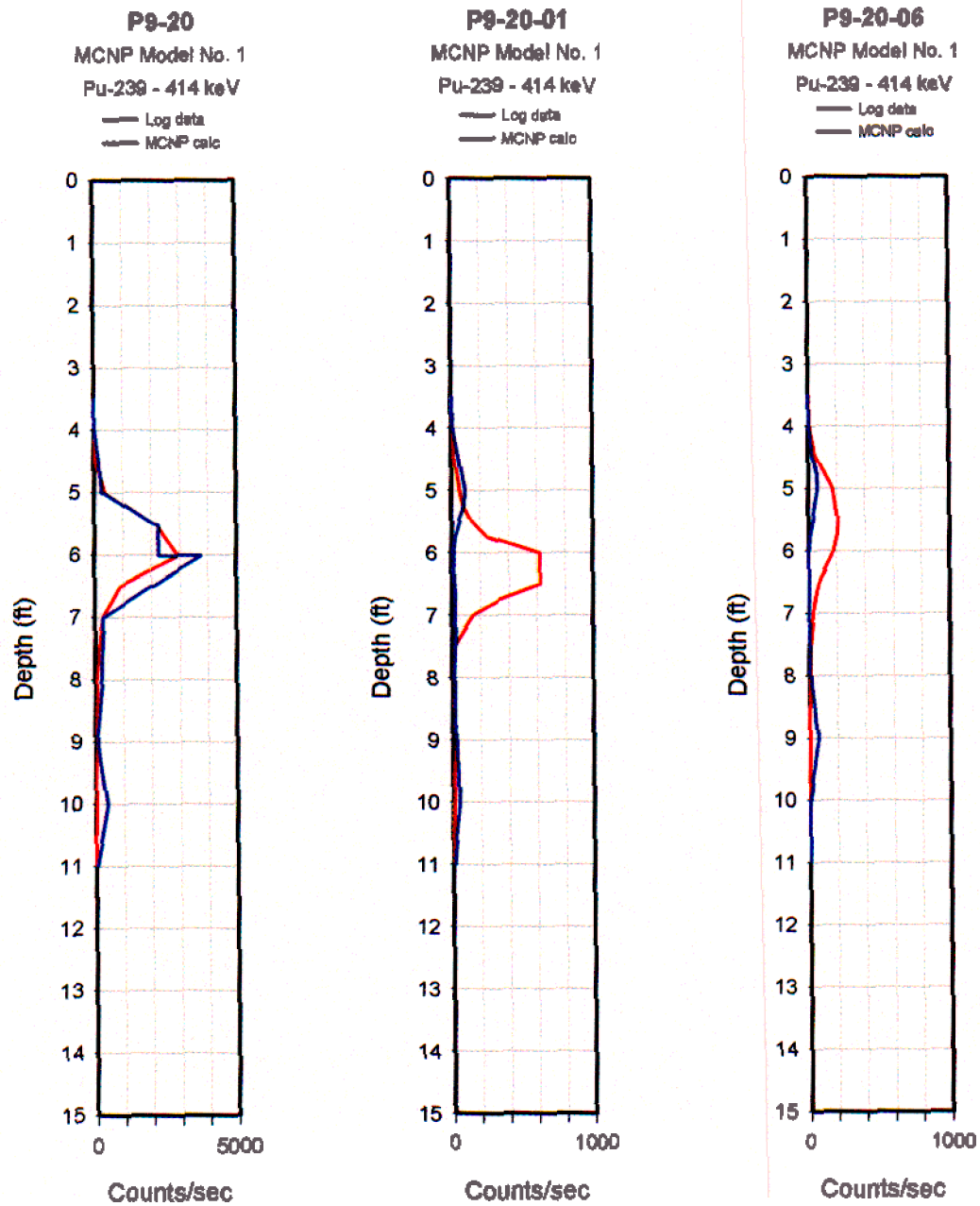


Figure 4. Plots of measured and MCNP calculated count rates for Model 1 probes.

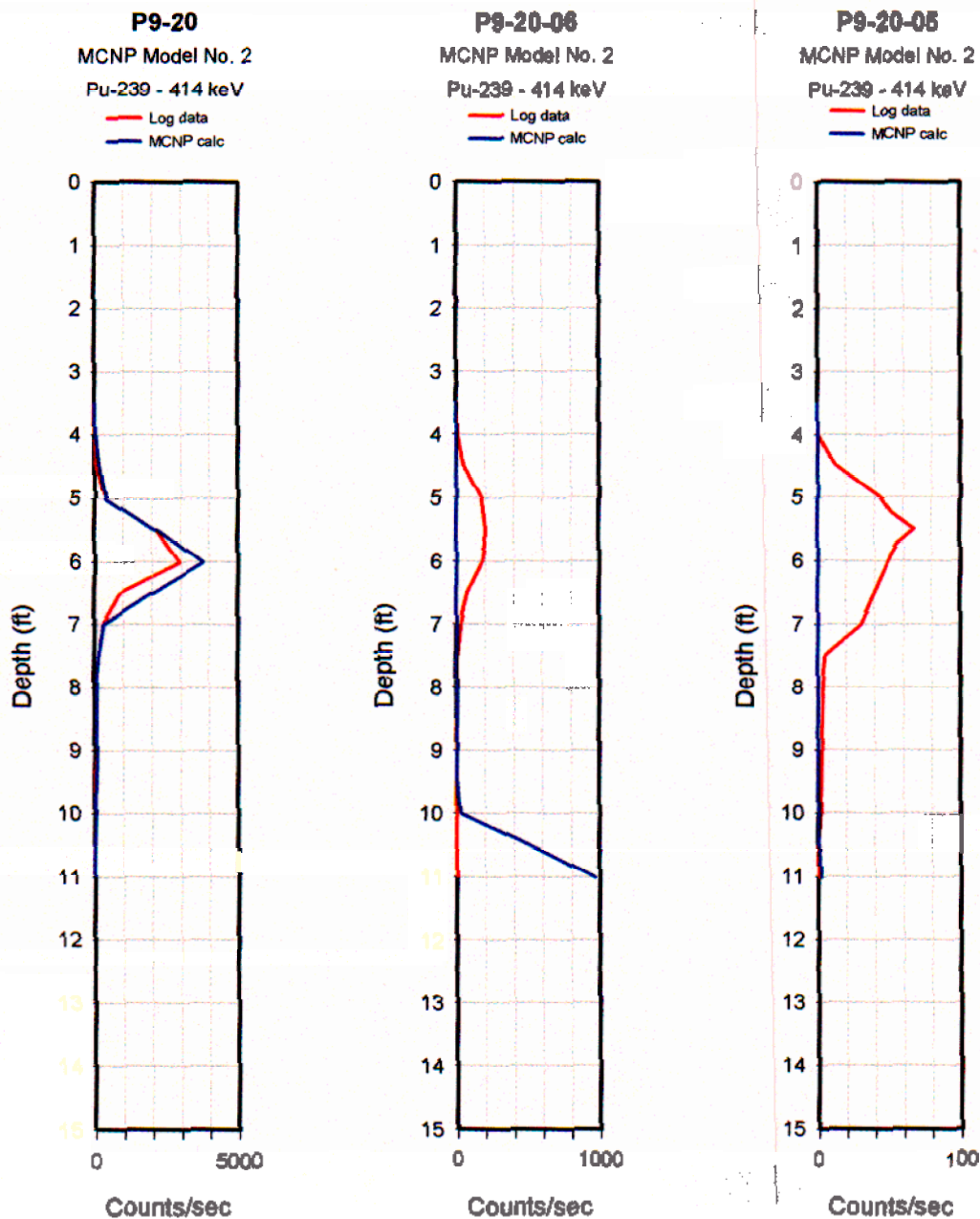


Figure 5. Plots of measured and MCNP calculated count rates for Model 2 probes.

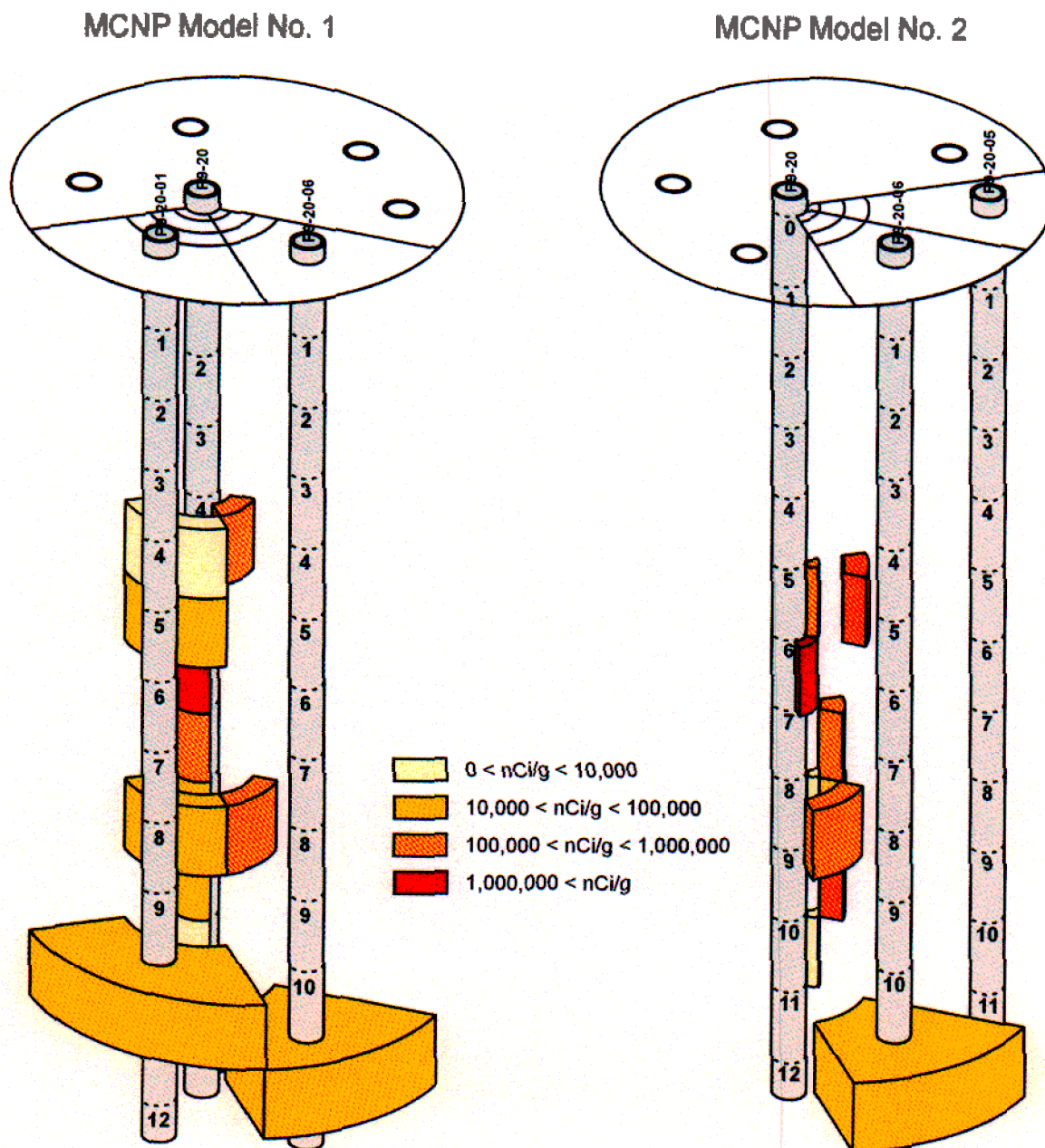


Figure 6. 3D visualization of Pu-239 source subvolumes.

Attachment C
Spreadsheet Model for Probe P9-20
N. Josten

Excel® Worksheet: P9-20

P9-20 x= 268169.0 y= 669483.2

Assumed Quantities

N_414	eps_414	area_d	r	t	dg	ds	azimuth	rho_w	rho_j	rho_s	kappa_w	kappa_l	kappa_s
1.51E-03	0.161	164	10	1.27	2.84	17.0	22.3	2	1.53	8	0.09411	0.09364	0.09071

6.20E-02 Pu specific activity (Ci/g)

5.3 sphere depth

268168.1 sphere x

669482.51 sphere y

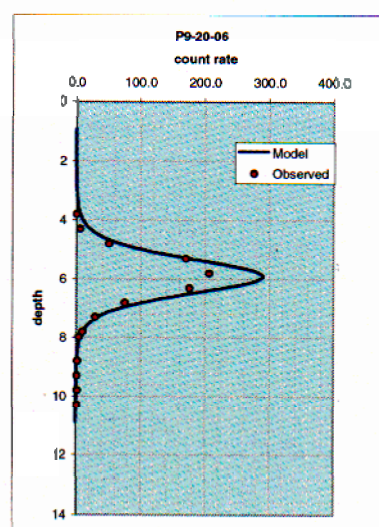
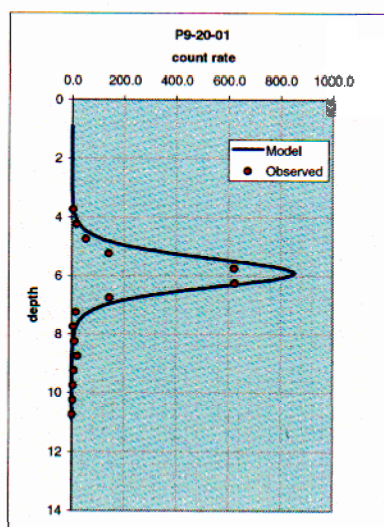
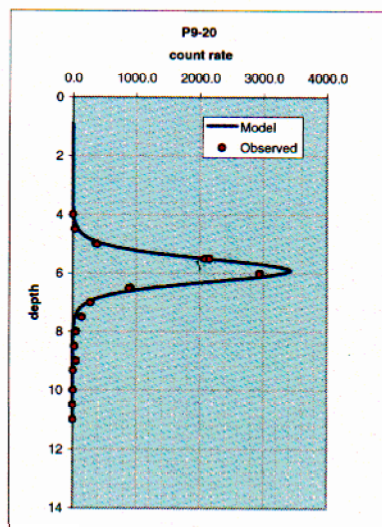
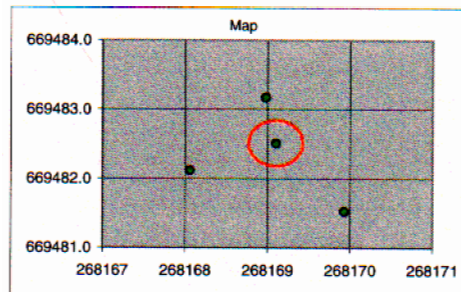
1.20E+07 sphere Pu concentration (nCi/g)

4.19E+03 waste volume (cc)

8.38E+03 waste mass (g)

1.01E+02 Pu activity (Ci)

1621.5 Pu mass (g)



Excel® Worksheet: P9-20 (continued)

												P9-20
h_feet	h_cm	depth	theta	L_w	L_i	L_s	L_g	term1	term2	Model	depth	Observed
5	152.40	0.9	80.8	154.4	63.23	7.97	17.81	986.63	3.6E-07	0.0	0.5	
4.8	146.30	1.1	80.5	148.4	60.78	7.66	17.12	1068.25	6.4E-07	0.0	1	
4.6	140.21	1.3	80.0	142.4	58.34	7.35	16.43	1160.33	1.1E-06	0.0	1.5	
4.4	134.11	1.5	79.6	136.4	55.90	7.04	15.73	1264.69	2.0E-06	0.0	2	
4.2	128.02	1.7	79.1	130.4	53.47	6.73	15.04	1383.61	3.6E-06	0.0	2.5	
4	121.92	1.9	78.6	124.4	51.04	6.42	14.35	1519.88	6.3E-06	0.0	3	
3.8	115.82	2.1	78.0	118.4	48.61	6.11	13.66	1676.99	1.1E-05	0.0	3.5	
3.6	109.73	2.3	77.4	112.5	46.19	5.80	12.98	1859.32	2.0E-05	0.0	4	2.94
3.4	103.63	2.5	76.6	106.5	43.78	5.50	12.29	2072.48	3.5E-05	0.1	4.5	34.48
3.2	97.54	2.7	75.8	100.6	41.37	5.19	11.61	2323.64	6.2E-05	0.1	5	362.86
3	91.44	2.9	74.9	94.7	38.98	4.89	10.93	2622.17	1.1E-04	0.3	5.01	382.19
2.8	85.34	3.1	73.9	88.8	36.59	4.58	10.25	2980.36	1.9E-04	0.6	5.5	2080.96
2.6	79.25	3.3	72.7	83.0	34.22	4.28	9.58	3414.63	3.3E-04	1.1	5.51	2156.84
2.4	73.15	3.5	71.4	77.2	31.86	3.98	8.91	3947.17	5.8E-04	2.3	6	2945.55
2.2	67.06	3.7	69.8	71.4	29.52	3.69	8.24	4608.40	1.0E-03	4.6	6.01	2939.12
2	60.96	3.9	68.0	65.7	27.21	3.39	7.59	5440.54	1.7E-03	9.4	6.5	911.47
1.8	54.86	4.1	65.8	60.1	24.93	3.10	6.94	6502.95	3.0E-03	19.2	6.51	887.85
1.6	48.77	4.3	63.2	54.6	22.70	2.82	6.30	7879.70	5.0E-03	39.4	7	283.02
1.4	42.67	4.5	60.0	49.3	20.52	2.54	5.68	9689.79	8.4E-03	81.0	7.01	278.14
1.2	36.58	4.7	56.1	44.1	18.41	2.27	5.09	12098.44	1.4E-02	166.0	7.5	141.00
1	30.48	4.9	51.1	39.2	16.42	2.02	4.52	15320.94	2.2E-02	336.2	7.51	142.31
0.8	24.38	5.1	44.7	34.6	14.58	1.79	4.00	19590.20	3.4E-02	663.1	8	52.31
0.6	18.29	5.3	36.6	30.7	12.96	1.58	3.54	25010.85	5.0E-02	1239.2	8.01	51.41
0.4	12.19	5.5	26.4	27.5	11.66	1.42	3.17	31171.77	6.7E-02	2097.0	8.5	29.07
0.2	6.10	5.7	13.9	25.4	10.80	1.31	2.93	36577.92	8.2E-02	3011.2	8.51	28.17
0	0.00	5.9	0.0	24.6	10.50	1.27	2.84	38822.25	8.8E-02	3431.7	9	53.09
-0.2	-6.10	6.1	-13.9	25.4	10.80	1.31	2.93	36577.92	8.2E-02	3011.2	9.01	54.31
-0.4	-12.19	6.3	-26.4	27.5	11.66	1.42	3.17	31171.77	6.7E-02	2097.0	9.32	8.08
-0.6	-18.29	6.5	-36.6	30.7	12.96	1.58	3.54	25010.85	5.0E-02	1239.2	10	10.45
-0.8	-24.38	6.7	-44.7	34.6	14.58	1.79	4.00	19590.20	3.4E-02	663.1	10.5	2.17
-1	-30.48	6.9	-51.1	39.2	16.42	2.02	4.52	15320.94	2.2E-02	336.2	11	0.14
-1.2	-36.58	7.1	-56.1	44.1	18.41	2.27	5.09	12098.44	1.4E-02	166.0	11.5	
-1.4	-42.67	7.3	-60.0	49.3	20.52	2.54	5.68	9689.79	8.4E-03	81.0	11.85	
-1.6	-48.77	7.5	-63.2	54.6	22.70	2.82	6.30	7879.70	5.0E-03	39.4		
-1.8	-54.86	7.7	-65.8	60.1	24.93	3.10	6.94	6502.95	3.0E-03	19.2		

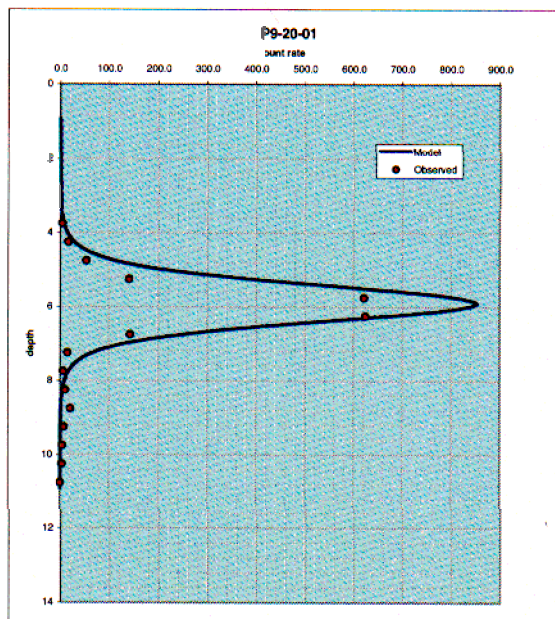
h_feet	h_cm	depth	theta	L_w	L_i	L_s	L_g	term1	term2	Model	P9-20	
											depth	Observed
-2	-60.96	7.9	-68.0	65.7	27.21	3.39	7.59	5440.54	1.7E-03	9.4		
-2.2	-67.06	8.1	-69.8	71.4	29.52	3.69	8.24	4608.40	1.0E-03	4.6		
-2.4	-73.15	8.3	-71.4	77.2	31.86	3.98	8.91	3947.17	5.8E-04	2.3		
-2.6	-79.25	8.5	-72.7	83.0	34.22	4.28	9.58	3414.63	3.3E-04	1.1		
-2.8	-85.34	8.7	-73.9	88.8	36.59	4.58	10.25	2980.36	1.9E-04	0.6		
-3	-91.44	8.9	-74.9	94.7	38.98	4.89	10.93	2622.17	1.1E-04	0.3		
-3.2	-97.54	9.1	-75.8	100.6	41.37	5.19	11.61	2323.64	6.2E-05	0.1		
-3.4	-103.63	9.3	-76.6	106.5	43.78	5.50	12.29	2072.48	3.5E-05	0.1		
-3.6	-109.73	9.5	-77.4	112.5	46.19	5.80	12.98	1859.32	2.0E-05	0.0		
-3.8	-115.82	9.7	-78.0	118.4	48.61	6.11	13.66	1676.99	1.1E-05	0.0		
-4	-121.92	9.9	-78.6	124.4	51.04	6.42	14.35	1519.88	6.3E-06	0.0		
-4.2	-128.02	10.1	-79.1	130.4	53.47	6.73	15.04	1383.61	3.6E-06	0.0		
-4.4	-134.11	10.3	-79.6	136.4	55.90	7.04	15.73	1264.69	2.0E-06	0.0		
-4.6	-140.21	10.5	-80.0	142.4	58.34	7.35	16.43	1160.33	1.1E-06	0.0		
-4.8	-146.30	10.7	-80.5	148.4	60.78	7.66	17.12	1068.25	6.4E-07	0.0		
-5	-152.40	10.9	-80.8	154.4	63.23	7.97	17.81	986.63	3.6E-07	0.0		

Excel® Worksheet: P9-20-01

x= 268168.1 y= 889482.1

quantities												
eps_414	area_d	r	t	dg	ds	rho_w	rho_i	rho_s	kappa_w	kappa_i	kappa_s	
0.161	164.0	10.0	1.27	2.84	16.96	2.00	1.53	8.00	0.09411	0.09364	0.09071	

Pu specific activity (Ci/g)
sphere depth
sphere Pu concentration (nCi/g)
waste volume (cc)
waste mass (g)
Pu activity (Ci)
Pu mass (g)



elev_corr: 0.1

Excel® Worksheet: P9-20-01 (continued)

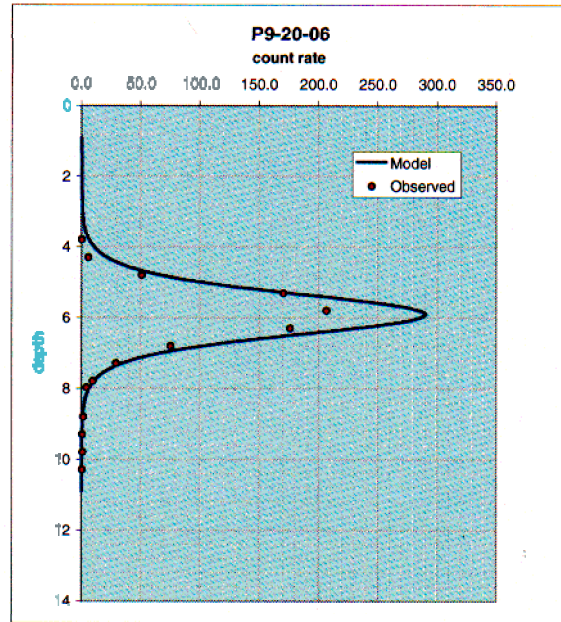
h_feet	h_cm	depth	theta	L_w	L_i	L_s	L_g	term1	term2	Model	depth	corr_ depth	P9-20-01 Observed
5	152.40	0.9	78.5	155.5	57.02	6.36	14.22	971.95	2.8E-06	0.0	0		
4.8	146.30	1.1	78.0	149.6	55.10	6.11	13.67	1051.06	4.4E-06	0.0	0.5	0.25	
4.6	140.21	1.3	77.5	143.6	53.18	5.87	13.13	1140.08	6.9E-06	0.0	1	0.75	
4.4	134.11	1.5	77.0	137.7	51.27	5.63	12.58	1240.67	1.1E-05	0.0	1.5	1.25	
4.2	128.02	1.7	76.4	131.7	49.36	5.38	12.04	1354.92	1.7E-05	0.0	2	1.75	
4	121.92	1.9	75.7	125.8	47.45	5.14	11.50	1485.32	2.7E-05	0.0	2.5	2.25	
3.8	115.82	2.1	75.0	119.9	45.56	4.90	10.96	1635.01	4.2E-05	0.1	3	2.75	
3.6	109.73	2.3	74.2	114.0	43.66	4.66	10.42	1807.87	6.5E-05	0.1	3.5	3.25	
3.4	103.63	2.5	73.3	108.2	41.78	4.42	9.89	2008.75	1.0E-04	0.2	4	3.75	4.69
3.2	97.54	2.7	72.3	102.4	39.91	4.18	9.36	2243.83	1.6E-04	0.4	4.5	4.25	17.42
3	91.44	2.9	71.2	96.6	38.04	3.95	8.83	2520.98	2.4E-04	0.6	5	4.75	53.34
2.8	85.34	3.1	70.0	90.8	36.19	3.71	8.30	2850.32	3.8E-04	1.1	5.5	5.25	141.26
2.6	79.25	3.3	68.6	85.1	34.36	3.48	7.78	3245.01	5.8E-04	1.9	6	5.75	622.10
2.4	73.15	3.5	67.0	79.5	32.54	3.25	7.26	3722.26	8.9E-04	3.3	6.5	6.25	624.71
2.2	67.06	3.7	65.1	73.9	30.75	3.02	6.75	4304.72	1.4E-03	5.9	7	6.75	143.20
2	60.96	3.9	63.0	68.4	28.98	2.80	6.25	5022.27	2.1E-03	10.4	7.5	7.25	15.07
1.8	54.86	4.1	60.5	63.1	27.26	2.58	5.76	5914.21	3.1E-03	18.4	8	7.75	6.20
1.6	48.77	4.3	57.5	57.8	25.57	2.36	5.29	7031.55	4.6E-03	32.4	8.5	8.25	10.62
1.4	42.67	4.5	53.9	52.8	23.95	2.16	4.82	8438.17	6.8E-03	57.0	9	8.75	21.65
1.2	36.58	4.7	49.6	48.0	22.41	1.96	4.39	10207.93	9.7E-03	99.2	9.5	9.25	8.33
1	30.48	4.9	44.4	43.5	20.97	1.78	3.98	12410.35	1.4E-02	169.1	10	9.75	4.96
0.8	24.38	5.1	38.1	39.5	19.68	1.61	3.61	15070.75	1.8E-02	278.7	10.5	10.25	4.20
0.6	18.29	5.3	30.5	36.1	18.57	1.47	3.30	18086.32	2.4E-02	434.2	11	10.75	0.29
0.4	12.19	5.5	21.4	33.4	17.71	1.36	3.05	21102.36	2.9E-02	620.4	11.5	11.25	
0.2	6.10	5.7	11.1	31.7	17.15	1.29	2.89	23448.50	3.3E-02	785.0	12	11.75	
0	0.00	5.9	0.0	31.1	16.96	1.27	2.84	24350.94	3.5E-02	852.6	12.5	12.25	

h_feet	h_cm	depth	theta	L_w	L_i	L_s	L_g	term1	term2	Model	depth	corr_ depth	P9-20-01 Observed
-0.2	-6.10	6.1	-11.1	31.7	17.15	1.29	2.89	23448.50	3.3E-02	785.0	13	12.75	
-0.4	-12.19	6.3	-21.4	33.4	17.71	1.36	3.05	21102.36	2.9E-02	620.4	13.41	13.16	
-0.6	-18.29	6.5	-30.5	36.1	18.57	1.47	3.30	18086.32	2.4E-02	434.2			
-0.8	-24.38	6.7	-38.1	39.5	19.68	1.61	3.61	15070.75	1.8E-02	278.7			
-1	-30.48	6.9	-44.4	43.5	20.97	1.78	3.98	12410.35	1.4E-02	169.1			
-1.2	-36.58	7.1	-49.6	48.0	22.41	1.96	4.39	10207.93	9.7E-03	99.2			
-1.4	-42.67	7.3	-53.9	52.8	23.95	2.16	4.82	8438.17	6.8E-03	57.0			
-1.6	-48.77	7.5	-57.5	57.8	25.57	2.36	5.29	7031.55	4.6E-03	32.4			
-1.8	-54.86	7.7	-60.5	63.1	27.26	2.58	5.76	5914.21	3.1E-03	18.4			
-2	-60.96	7.9	-63.0	68.4	28.98	2.80	6.25	5022.27	2.1E-03	10.4			
-2.2	-67.06	8.1	-65.1	73.9	30.75	3.02	6.75	4304.72	1.4E-03	5.9			
-2.4	-73.15	8.3	-67.0	79.5	32.54	3.25	7.26	3722.26	8.9E-04	3.3			
-2.6	-79.25	8.5	-68.6	85.1	34.36	3.48	7.78	3245.01	5.8E-04	1.9			
-2.8	-85.34	8.7	-70.0	90.8	36.19	3.71	8.30	2850.32	3.8E-04	1.1			
-3	-91.44	8.9	-71.2	96.6	38.04	3.95	8.83	2520.98	2.4E-04	0.6			
-3.2	-97.54	9.1	-72.3	102.4	39.91	4.18	9.36	2243.83	1.6E-04	0.4			
-3.4	-103.63	9.3	-73.3	108.2	41.78	4.42	9.89	2008.75	1.0E-04	0.2			
-3.6	-109.73	9.5	-74.2	114.0	43.66	4.66	10.42	1807.87	6.5E-05	0.1			
-3.8	-115.82	9.7	-75.0	119.9	45.56	4.90	10.96	1635.01	4.2E-05	0.1			
-4	-121.92	9.9	-75.7	125.8	47.45	5.14	11.50	1485.32	2.7E-05	0.0			
-4.2	-128.02	10.1	-76.4	131.7	49.36	5.38	12.04	1354.92	1.7E-05	0.0			
-4.4	-134.11	10.3	-77.0	137.7	51.27	5.63	12.58	1240.67	1.1E-05	0.0			
-4.6	-140.21	10.5	-77.5	143.6	53.18	5.87	13.13	1140.08	6.9E-06	0.0			
-4.8	-146.30	10.7	-78.0	149.6	55.10	6.11	13.67	1051.06	4.4E-06	0.0			
-5	-152.40	10.9	-78.5	155.5	57.02	6.36	14.22	971.95	2.8E-06	0.0			

Excel® Worksheet: P9-20-06

6.20E-02 Pu specific activity (Ci/g)
5.9 sphere depth
1.20E+07 sphere Pu concentration (nCi/g)
41
12 PL
1621.5 PL

rho_w	rho_i	rho_s	kappa_w	kappa_i	kappa_s
2.00	1.53	8.00	0.09411	0.09364	0.09071



elev_corr: 0.2
0.3

Excel® Worksheet: P9-20-06 (continued)

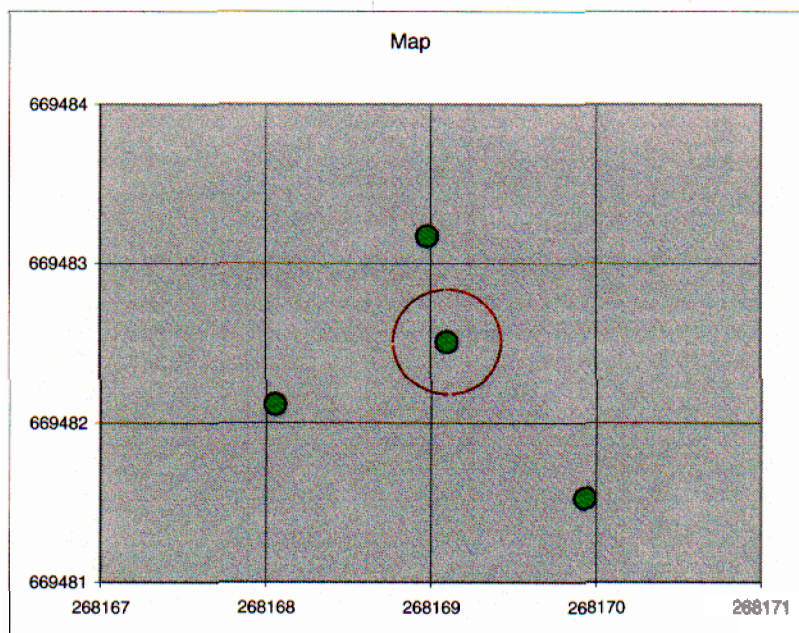
h_feet	h_cm	depth	theta	L_w	L_i	L_s	L_g	term1	term2	Model	depth	depth_ corr	P9-20-06 Observed
5	152.40	0.9	76.6	156.7	55.34	5.47	12.23	957.78	6.8E-06	0.0	0.5	0.8	
4.8	146.30	1.1	76.0	150.8	53.71	5.26	11.77	1034.52	1.0E-05	0.0	1.0	1.3	
4.6	140.21	1.3	75.5	144.9	52.09	5.06	11.31	1120.63	1.5E-05	0.0	1.5	1.8	
4.4	134.11	1.5	74.8	139.0	50.47	4.85	10.85	1217.68	2.1E-05	0.0	2.0	2.3	
4.2	128.02	1.7	74.1	133.1	48.85	4.65	10.39	1327.54	3.1E-05	0.0	2.5	2.8	
4	121.92	1.9	73.4	127.2	47.24	4.44	9.93	1452.49	4.6E-05	0.1	3.0	3.3	
3.8	115.82	2.1	72.6	121.4	45.64	4.24	9.48	1595.32	6.7E-05	0.1	3.5	3.8	0.3
3.6	109.73	2.3	71.7	115.6	44.05	4.04	9.02	1759.46	9.7E-05	0.2	4.0	4.3	5.9
3.4	103.63	2.5	70.7	109.8	42.46	3.83	8.57	1949.17	1.4E-04	0.3	4.5	4.8	51.1
3.2	97.54	2.7	69.5	104.1	40.88	3.63	8.13	2169.74	2.0E-04	0.4	5.0	5.3	170.7
3	91.44	2.9	68.3	98.4	39.32	3.44	7.68	2427.83	3.0E-04	0.7	5.5	5.8	206.9
2.8	85.34	3.1	66.9	92.8	37.77	3.24	7.24	2731.82	4.3E-04	1.2	6.0	6.3	176.2
2.6	79.25	3.3	65.3	87.2	36.24	3.04	6.81	3092.30	6.1E-04	1.9	6.5	6.8	75.5
2.4	73.15	3.5	63.6	81.7	34.73	2.85	6.38	3522.71	8.7E-04	3.1	7.0	7.3	29.4
2.2	67.06	3.7	61.5	76.3	33.24	2.66	5.96	4040.06	1.2E-03	5.0	7.5	7.8	9.7
2	60.96	3.9	59.2	71.0	31.78	2.48	5.54	4665.67	1.7E-03	8.1	7.7	8.0	4.4
1.8	54.86	4.1	56.5	65.8	30.36	2.30	5.14	5425.86	2.4E-03	13.2	8.5	8.8	1.9
1.6	48.77	4.3	53.3	60.8	28.99	2.12	4.75	6351.85	3.4E-03	21.4	9.0	9.3	1.0
1.4	42.67	4.5	49.6	56.1	27.68	1.96	4.38	7477.90	4.6E-03	34.2	9.5	9.8	1.1
1.2	36.58	4.7	45.2	51.6	26.45	1.80	4.03	8835.38	6.1E-03	54.1	10.0	10.3	0.7
1	30.48	4.9	40.0	47.5	25.31	1.66	3.71	10438.83	8.0E-03	83.4	10.5	10.8	
0.8	24.38	5.1	33.8	43.8	24.31	1.53	3.42	12259.12	1.0E-02	124.2	11.0	11.3	
0.6	18.29	5.3	26.7	40.7	23.46	1.42	3.18	14182.66	1.2E-02	175.4	11.5	11.8	
0.4	12.19	5.5	18.5	38.4	22.82	1.34	3.00	15972.84	1.4E-02	230.0	11.9	12.2	
0.2	6.10	5.7	9.5	36.9	22.41	1.29	2.88	17281.64	1.6E-02	273.8			
0	0.00	5.9	0.0	36.4	22.27	1.27	2.84	17766.91	1.6E-02	290.9			

h_feet	h_cm	depth	theta	L_w	L_i	L_s	L_g	term1	term2	Model	depth	depth_ corr	P9-20-06 Observed
-0.2	-6.10	6.1	-9.5	36.9	22.41	1.29	2.88	17281.64	1.6E-02	273.8			
-0.4	-12.19	6.3	-18.5	38.4	22.82	1.34	3.00	15972.84	1.4E-02	230.0			
-0.6	-18.29	6.5	-26.7	40.7	23.46	1.42	3.18	14182.66	1.2E-02	175.4			
-0.8	-24.38	6.7	-33.8	43.8	24.31	1.53	3.42	12259.12	1.0E-02	124.2			
-1	-30.48	6.9	-40.0	47.5	25.31	1.66	3.71	10438.83	8.0E-03	83.4			
-1.2	-36.58	7.1	-45.2	51.6	26.45	1.80	4.03	8835.38	6.1E-03	54.1			
-1.4	-42.67	7.3	-49.6	56.1	27.68	1.96	4.38	7477.90	4.6E-03	34.2			
-1.6	-48.77	7.5	-53.3	60.8	28.99	2.12	4.75	6351.85	3.4E-03	21.4			
-1.8	-54.86	7.7	-56.5	65.8	30.36	2.30	5.14	5425.86	2.4E-03	13.2			
-2	-60.96	7.9	-59.2	71.0	31.78	2.48	5.54	4665.67	1.7E-03	8.1			
-2.2	-67.06	8.1	-61.5	76.3	33.24	2.66	5.96	4040.06	1.2E-03	5.0			
-2.4	-73.15	8.3	-63.6	81.7	34.73	2.85	6.38	3522.71	8.7E-04	3.1			
-2.6	-79.25	8.5	-65.3	87.2	36.24	3.04	6.81	3092.30	6.1E-04	1.9			
-2.8	-85.34	8.7	-66.9	92.8	37.77	3.24	7.24	2731.82	4.3E-04	1.2			
-3	-91.44	8.9	-68.3	98.4	39.32	3.44	7.68	2427.83	3.0E-04	0.7			
-3.2	-97.54	9.1	-69.5	104.1	40.88	3.63	8.13	2169.74	2.0E-04	0.4			
-3.4	-103.63	9.3	-70.7	109.8	42.46	3.83	8.57	1949.17	1.4E-04	0.3			
-3.6	-109.73	9.5	-71.7	115.6	44.05	4.04	9.02	1759.46	9.7E-05	0.2			
-3.8	-115.82	9.7	-72.6	121.4	45.64	4.24	9.48	1595.32	6.7E-05	0.1			
-4	-121.92	9.9	-73.4	127.2	47.24	4.44	9.93	1452.49	4.6E-05	0.1			
-4.2	-128.02	10.1	-74.1	133.1	48.85	4.65	10.39	1327.54	3.1E-05	0.0			
-4.4	-134.11	10.3	-74.8	139.0	50.47	4.85	10.85	1217.68	2.1E-05	0.0			
-4.6	-140.21	10.5	-75.5	144.9	52.09	5.06	11.31	1120.63	1.5E-05	0.0			
-4.8	-146.30	10.7	-76.0	150.8	53.71	5.26	11.77	1034.52	1.0E-05	0.0			
-5	-152.40	10.9	-76.6	156.7	55.34	5.47	12.23	957.78	6.8E-06	0.0			

Excel® Worksheet: Map

Point x y
P9-20 268169.0 669483.2
P9-20-01 268168.1 669482.1
P9-20-06 268169.9 669481.5
Sphere 268169.1 669482.5

radius 10



	x	y		x	y		x	y		x	y
0	268169.4	669482.5	95	268169.1	669482.8	185	268168.8	669482.5	275	268169.1	669482.2
5	268169.4	669482.5	100	268169	669482.8	190	268168.8	669482.5	280	268169.2	669482.2
10	268169.4	669482.6	105	268169	669482.8	195	268168.8	669482.4	285	268169.2	669482.2
15	268169.4	669482.6	110	268169	669482.8	200	268168.8	669482.4	290	268169.2	669482.2
20	268169.4	669482.6	115	268169	669482.8	205	268168.8	669482.4	295	268169.2	669482.2
25	268169.4	669482.6	120	268168.9	669482.8	210	268168.8	669482.3	300	268169.3	669482.2
30	268169.4	669482.7	125	268168.9	669482.8	215	268168.8	669482.3	305	268169.3	669482.2
35	268169.4	669482.7	130	268168.9	669482.8	220	268168.8	669482.3	310	268169.3	669482.3
40	268169.4	669482.7	135	268168.9	669482.7	225	268168.9	669482.3	315	268169.3	669482.3
45	268169.3	669482.7	140	268168.8	669482.7	230	268168.9	669482.3	320	268169.4	669482.3
50	268169.3	669482.8	145	268168.8	669482.7	235	268168.9	669482.2	325	268169.4	669482.3
55	268169.3	669482.8	150	268168.8	669482.7	240	268168.9	669482.2	330	268169.4	669482.3
60	268169.3	669482.8	155	268168.8	669482.6	245	268169	669482.2	335	268169.4	669482.4
65	268169.2	669482.8	160	268168.8	669482.6	250	268169	669482.2	340	268169.4	669482.4
70	268169.2	669482.8	165	268168.8	669482.6	255	268169	669482.2	345	268169.4	669482.4
75	268169.2	669482.8	170	268168.8	669482.6	260	268169	669482.2	350	268169.4	669482.5
80	268169.2	669482.8	175	268168.8	669482.5	265	268169.1	669482.2	355	268169.4	669482.5
85	268169.1	669482.8	180	268168.8	669482.5	270	268169.1	669482.2	360	268169.4	669482.5
90	268169.1	669482.8									